Push Recovery Control of Bipedal Robots

by

Ibrahim Altameemi

A Thesis

Submitted to the Faculty

of the
WORCESTER POLYTECHNIC INSTITUTE

In partial fulfillment of the requirements for the
Degree of Master of Science
in
Robotics Engineering

by
December 2023

APPROVED:
Professor Mahdi Agheli, Major Thesis Advisor
Professor Jing Xiao, Committee Member
Professor Andre Rosendo, Committee Member

Abstract

Bipedal robots are expected to play a crucial role in daily life, supporting humans with tasks, functioning in industrial facilities, providing healthcare, and executing search and rescue missions in hazardous situations. Bipedal robots are complex mechanical machines requiring extensive research. Bipedal robots struggle to maintain balance in the presence of external disturbances, which limits their interaction with their surroundings. Therefore, developing a robust push recovery control is essential for these robots to maintain balance while executing the planned tasks.

The objective of this work is to develop a push recovery control system that maintains the stability of the momentum's rate of change (**Disturbance Avoidance Phase**) and subsequently restores our robot (HURON) to an upright position once the disturbance subsides (**Posture Recovery Phase**). We develop and validate a reaching law-based Sliding Mode Control (SMC) to stabilize the rate of change of linear momentum. The proposed SMC incorporates a **Variable Power Rate Reaching Law ($\dot{s}$)**, dynamically adjusting to changes in the system. The study examines angular momentum regulation through two approaches, considering the CoP position, CoM position, the desired rate of change of linear momentum, and Ground Reaction Forces. This study also proposes using the null-space method to restore the robot to the upright posture without interfering with its main momentum controllers. The **Higher Priority** task is for the momenta controllers (**Disturbance Avoidance Phase**), while the **Lower Priority** task is (**Posture Recovery Phase**).

The simulation results illustrate that the proposed push recovery control effectively preserved standing stability in the presence of external disturbances. Moreover, the proposed control method reduces chattering in joint torques and eliminates oscillations. Additionally, the results show that the push recovery control, when implemented using the **Second Approach** of angular momentum controller, yields smaller CoP position values than the **First Approach**. This study also involves conducting experiments where two successive pushing forces are applied to our robot (HURON) within a short time. The robot demonstrates remarkable stability, even under the influence of these forces. This stability can be attributed to the effective implementation of the null-space method, allowing the performing of both the **Disturbance Avoidance Phase** and **Posture Recovery Phase** simultaneously. A comparison with established controllers shows the superiority of the proposed approach, particularly in reducing the CoP peak.

This thesis additionally presents our ongoing research focusing on the stepping strategy. If the robot cannot maintain its standing stability when subjected to a large pushing force, it must take a step. Our methodology involves selecting the step position based on variations in momenta. Subsequently, the desired CoM and swing leg trajectories are generated using a quadratic Bezier curve and a Gaussian function. A multi-objective optimization problem is employed to minimize the momenta and swing leg trajectory errors while considering stability constraints. The experimental stage is currently in progress. Initial findings indicate promising results; nevertheless, a thorough examination and explanation are still needed. The ongoing data collection and analysis processes will yield conclusive results in the coming days, further validating the efficacy of the employed methodology. Our future plans include implementing our proposed push recovery control to our manufactured bipedal, HURON, once it is ready for experimental tests. Additionally, we plan to complete the current work related to push recovery via stepping.

Acknowledgements

I want to thank my adviser, Professor Mahdi Agheli, for his essential advice, persistent support, and insightful feedback during my research. Moreover, I want to convey my deep appreciation for the tremendous support the Fulbright scholarship provides, which has significantly enhanced my scientific and cultural knowledge.

I thank my committee members, Prof. Jing Xiao and Prof. Andre Rosendo. I appreciate your time reading my thesis and providing advice to enhance it.

I sincerely appreciate my hardworking teammates (Thai Duc, Abizer Patanwala, Hushmand Esmaeili, Ethan Chandler, Nhi Nguyen, Zhun Cheng, Sahen Juneja, Carlos G, Dheeraj Bhogisetty and Nikhil Gangaram). Your willingness to work together, wide range of expertise, and combined effort have been invaluable to our research. This academic path has been fulfilling and fun because of the friendships formed and the common desire for greatness.

I would want to express my gratitude to best friends Diyar Aljabbari, Jordan J. Jones, Oger Zaya, M. Kareem, and Yahya Ghufran. Thank you very much for your motivation and friendship.

Contents

List of Tables

List of Figures

List of Acronyms

ZMP: Zero Moment Point

CoP: Center of Pressure

CoM: Center of Mass

LIPM: *Linear Inverted pendulum Model*

SMC: Sliding Model Control

GRF: Ground Reaction Force

LQR: Linear Quadratic Regulator

VMC: Virtual Model Control

PD: Proportional-Derivative

F/T: Force/Torque

DBFC: Dynamic Balance Force Control

DoF: Degrees of Freedom

FSR: Force Sensing Resistor

CAN: Controller Area Network

CTC: Computed Torque Control

EERL: Enhanced Exponential Reaching Law

ERL: Exponential Reaching Law

CRL: Constant Reaching Law

CPRL: Constant Power Reaching Law

PRL: Power Reaching Law

DE: Double-Exponential

LPF: Low Pass Filter

LDIP: Linearized Double Inverted Pendulum

CP: Capture Point

ODE: Open Dynamics Engine

ICP: Instantaneous Capture Point

MPC: Model Predictive Control

CMM: Centroidal Momentum Matrix

IK: Inverse Kinematics

1 Introduction

The development of bipedal robots began around three decades ago. Over the past twenty years, there has been a significant increase in research conducted on bipedal robots. This advancement results from significant advances in various fields, including material sciences, mechanical engineering, software engineering, and perception. Bipedal robots' ability to maintain balance has been and will continue to be one of the research hotspots. Despite this, the challenge of successfully developing controllers that can keep the system in balance despite disturbances is still difficult. This thesis focuses on designing a *momentum-based balance control system* for our bipedal robot (HURON), depicted in Fig. 1.

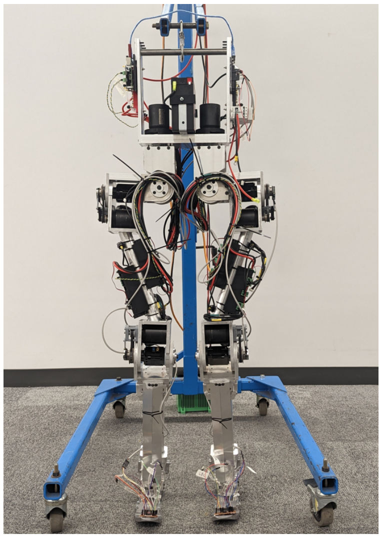

Figure 1: Our bipedal robot (HURON).

1.1 Motivation

Bipedal robots are expected to become essential elements of our daily lives, fulfilling various duties, including assisting humans in everyday jobs, operating in industrial facilities, delivering healthcare services, and conducting search and rescue missions in dangerous environments. Bipedal robots are highly complex mechanical machines that require significant research in this field. An important limitation that restricts the ability of bipedal robots to interact with their environment is their inadequate capability to maintain balance in the presence of external disturbances. Therefore, it is crucial to develop a robust push recovery control system that allows these robots to preserve balance while executing the planned tasks. This has been the primary motivation of this study.

1.2 Problem Statement

Several studies have investigated the use of *momentum-based balance control* with simple controllers, such as Proportional-Derivative (PD) controllers, to stabilize the motion of the Center of Mass (CoM), which is equivalent to regulating the linear momentum. Other studies used the Proportional Linear Momentum Rate Controller, where the desired rate of change of linear momentum is defined as a proportional function of the current linear momentum. However, when it comes to stabilizing the linear momentum of a bipedal robot in order to achieve balance, simple controllers are not an effective solution due to the complex, nonlinear, and coupled dynamics of bipedal motion. Moreover, the desired rate of change of angular momentum was either assumed to be zero or defined only in terms of the Center of Pressure (CoP) without considering the desired rate of change of linear momentum or the Ground Reaction Force (GRF). The push recovery process can be divided into two distinct phases: the **Disturbance Avoidance Phase**, which aims to stabilize the rate of change of momenta, and the **Posture Recovery Phase**, which focuses on returning the robot to an upright position after the disturbance subsides. These phases must operate simultaneously to ensure optimal performance. However, it has been observed that these phases are often executed sequentially, meaning that the **Disturbance Avoidance Phase** runs first, followed by the **Posture Recovery Phase**. Thus, attempting to exert force to the robot while it is restoring its posture will not properly maintain its momentum, resulting in a fall.

1.3 Research Goal

The aim of this work is to develop a push recovery control system that stabilizes the rate of change of momenta (**Disturbance Avoidance Phase**) and then restores our robot (HURON) to an upright position after the disturbance diminishes (**Posture Recovery Phase**). The phases must operate simultaneously to provide efficiency in performance .

1.4 Contribution

Our specific contributions include:

1) Designing and validating an improved reaching law-based Sliding Mode Control (SMC) for stabilizing the linear momentum of bipedal robots. The proposed reaching law can eliminate chattering and allow the system to approach the sliding mode surface from any point in a short period, as will be explained in section 4.2.1.

2) Defining the desired rate of change of angular momentum about the Center of Mass (CoM) in a way that incorporates the desired rate of change of linear momentum, the difference between the positions of the CoP and CoM, and the normal component of the Ground Reaction Force ($F_{GR,z}$), as will be discussed in section 4.2.2.

3) Introducing a null-space method for restoring the robot's upright posture during the **Posture Recovery Phase** without interfering with primary momentum controllers, as will be explained in section 4.3.

Moreover, we compare our proposed push recovery control (*Standing Stability*) with those presented in [6], [5], and other established controllers, highlighting the advantages of our approach.

1.4.1 Publication List

1- " Push Recovery Control of Bipedal Robots Using an Improved Reaching Law-Based Sliding Mode Control and Null-Space Method." Submitted to International Conference on Robotics and Automation (ICRA), 2024.

2- " Momentum-Based Push Recovery Control for Bipedal Robots: Integrating Standing and Stepping Balance." In preparation for submission to IEEE Access by March 1, 2024.

1.5 Structure of the Thesis

The structure of this thesis is as follows:

Section 2 presents a comprehensive analysis of the biomechanics of standing balance. Subsequently, it thoroughly analyzes the three balance strategies (*Ankle*, *Hip*, and *Step*), along with their corresponding stability regions. Lastly, this section provides an overview of bipedal balance control strategies including momentum-based strategies.

Section 3 introduces our bipedal robot (HURON), which is utilized as the platform for implementing our proposed push recovery controller.

Section 4 provides the proposed push recovery control, which aims to maintain standing stability. The proposed control incorporates a Sliding Mode Control with **Variable Power Rate Reaching Law** to stabilize the rate of change in linear momentum. This section also shows how we define the rate of change of angular momentum using two approaches. Additionally, it demonstrates the utilization of the null-space method for recovering an upright posture.

Section 5 initially displays the outcomes of the proposed push recovery control, as explained in section 4.2.2. Additionally, it presents a comparative analysis of the stability performance of the proposed control method against other well-recognized controllers.

Section 6 presents the conclusions that can be drawn on this research.

Section 7 shows our ongoing study, focusing on the implementation methodology of the push recovery control by stepping. As of the current stage, conclusive results are not available. This section initially clarifies the process of determining the step position based on momenta. In section 7.1.2.2, the required linear and angular momenta, as well as the trajectory of the swing leg, are generated. Section 7.1.2.3 presents the objective function and the necessary constraints for taking a step while maintaining stability. Additionally, this section presents potential opportunities for future research.

2 Background

Section 2.1 will provide an overview of the standing balance biomechanics. In sections 2.2 and 2.3, the *Ankle Strategy* and *Hip Strategy* with their corresponding stability regions will be discussed. Section 2.4 will highlight the *Step Strategy.* Section 2.5 will provide the basic concepts of static and dynamic balance of bipedal robots. In section 2.6, we will give a brief overview of bipedal balance control strategies (*Ankle/Hip strategy* and *Momentum-Based Strategy*). Later on, we will highlight our contribution to advancing the development of the *Momentum-Based Strategy.*

2.1 The Biomechanics of Balance

According to biomechanics research, it has been observed that the human body is considered to be an unstable system due to the concentration of approximately two-thirds of its total mass at a height that is also about two-thirds above the ground [1]. Therefore, humans need to use an active control strategy to ensure stability. The author of [1] identified three primary sensory systems contributing to balance and posture. Vision is primarily responsible for planning our movement and avoiding obstacles along the path. The vestibular system is our "gyro" that detects linear and angular accelerations. Multiple sensors in the somatosensory system detect the position and velocity of all body segments, their contact (impact) with external objects (including the ground), and the orientation of gravity.

The essential component of quiet standing is the difference between the Center of Pressure (CoP) and the Center of Mass (CoM). Assuming the body to be an inverted pendulum, pivoting about the ankle joint as shown in Fig. 2, a counterclockwise moment equal to RP and a clockwise moment equal to Wg will be acting [1].

$$I\alpha = RP - Wg \tag{1}$$

where I is the moment of inertia of the total body about the ankle joint, α is the angular acceleration of the inverted pendulum, W is the body weight, and R is the vertical reaction force. P and g represent the distance from the pivot point (ankle joint) to the CoP and CoM, respectively.

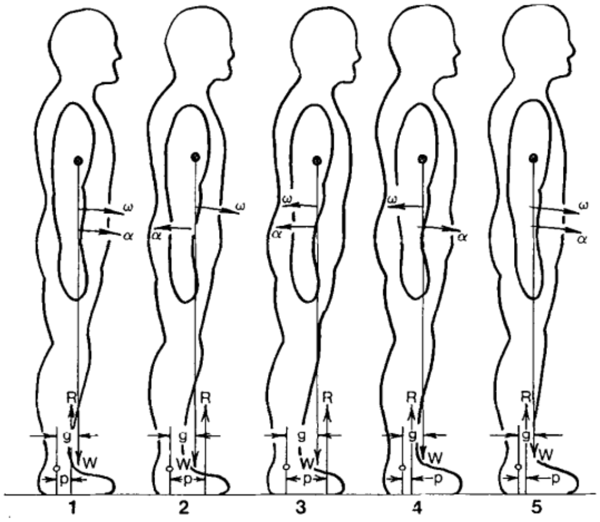

Figure 2: A subject swaying back and forth while standing quietly on a force platform [1]. w is the angular velocity.

In Fig. 2, it can be shown that when $Wg > RP$, the body exhibits a clockwise rotational motion. In order to correct this motion, the individual must manipulate the position of the CoP by increasing the degree of plantar flexion exhibited at the ankle joint [1]. Consequently, the CoP will be positioned anterior (towards the front) to the CoM, while the $Wg < RP$, as depicted in time 2 of Fig. 2. Currently, the angular acceleration, denoted as α, will induce a counterclockwise rotation, resulting in a decrease in the angular velocity, represented as w, of the object. This behavior persists until time 3, during which both α and w exhibit counterclockwise motion, resulting in the backward movement of the body. The CoP shifts posteriorly (towards the back) in response to a decrease in plantar flexion activity, ultimately aligning itself behind the CoM. When this event occurs, the central nervous system detects the posterior displacement of the CoM and initiates corrective action by activating the forward rotation of α at time 4. Over time, the value of w will decrease and reverse its direction, leading to the body returning to its initial position observed at time 5. This sequence shows the importance of the CoP and CoM positions in maintaining quiet standing.

In quiet standing, the *Ankle Strategy* is employed in response to minor disturbances. In more perturbed situations or when the ankle muscles cannot act, a *Hip Strategy* would respond by flexing the hip and shifting the CoM anteriorly. The impact of *Ankle Strategy* and *Hip Strategy* on CoM displacement is depicted in Fig. 3. In the presence of forward perturbations, the combined

Ankle and *Hip Strategy* can drive the CoM more backward compared to the *Ankle Strategy* or *Hip Strategy* alone, according to the study conducted by [1]. This indicates that the combined strategy can handle larger perturbations than only the *Ankle* or *Hip Strategy.* If the combined *Ankle* and *Hip Strategy* cannot withstand the perturbations, humans must move a limb forward to stop their forward fall (*Step Strategy*).

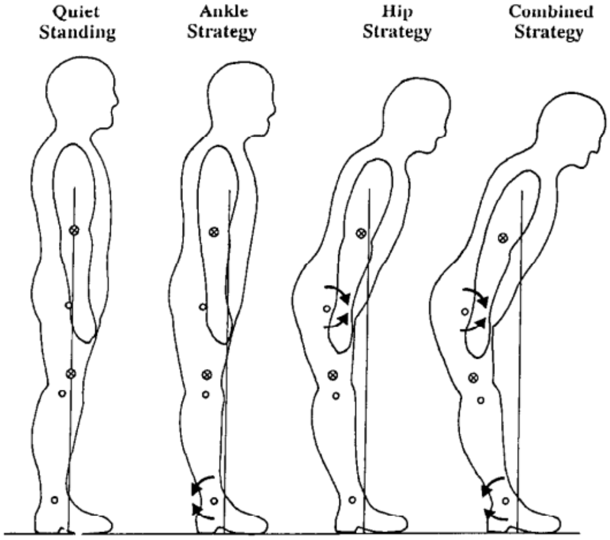

Figure 3: Displacement of the CoM of the body as a result of an external perturbation with the *Ankle Strategy*, *Hip Strategy* and *Ankle* and *Hip* combined strategy [1].

2.2 Ankle Strategy

Research in the field of biomechanics has yielded evidence suggesting that humans frequently utilize the *Ankle Strategy* to maintain balance in response to minor perturbations. The diagram in Fig. 4a illustrates the *Ankle Strategy*, which shows how a disturbance causes a deviation of the CoM from its desired position. The *Ankle Strategy* refers to restricting movement in the hip and knee joints while employing torque in the ankle joint to reposition the CoM to the desired position. Using solely ankle torque allows applying the *Linear Inverted Pendulum Model (LIPM)* as a simplified model for investigating the *Ankle Strategy.*

Linear Inverted Pendulum Model (LIPM): A system of rigid bodies can be approximated as a single mass. At each instant, the sum of forces acting on a system causes a change in linear momentum $\dot{L}$ or, equivalently, an acceleration of the system's CoM. Simultaneously, the

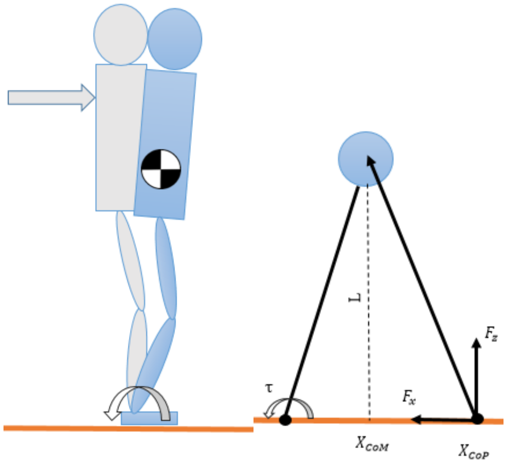

(a) (b)

Figure 4: (a) The *Ankle Strategy*, (b) The *Linear Inverted Pendulum Model (LIPM).*

sum of moments about the CoM results in a change in the system's angular momentum $\dot{H}$ about the COM. In the *LIPM* in (xz plane), it is presumed that the system has no angular momentum $H_{CoM,y} = 0$ and that there is no change in angular momentum $\dot{H}_{CoM,y} = 0$. This indicates that the system's forces do not generate moments about the CoM. Additionally, in the *LIPM*, the height of the CoM is also presumed to be constant. The dynamics of the planar *LIPM* in the sagittal direction (sagittal and frontal planes are illustrated in appendix A) described in Fig. 4b can be expressed as

$$m\ddot{x}_{CoM} = \frac{mg}{z_0}(x_{CoM} - x_{CoP}) \tag{2}$$

$$\dot{x}_{CoP} = u \tag{3}$$

where x_{CoM} is the CoM horizontal position, at a constant height z_0, x_{CoP} is the CoP position, m is the system's total mass, g is the acceleration due to gravity, and u is the control input for the CoP. Notably, the same dynamics are in the frontal direction. As shown in Fig. 4b, to satisfy the assumption that there is no change in angular momentum about the CoM ($H_{CoM,y} = 0$), the Ground Reaction Force (GRF) must point from the CoP in the direction of the CoM. Thus, *Ankle Strategy* is also called CoP balancing [9]. This indicates that in the *Ankle Strategy*, the CoP position is regulated to maintain stability. As known, the range of CoP position is constrained by the dimensions of the support polygon. This CoP constraint imposes a constraint on the torque of the ankle joint, as described in equation 4, which was derived by [10].

$$x_{CoP} = \frac{F_T - \tau}{F_N} \tag{4}$$

where τ is the ankle torque, F_N is equal to mg, which is the normal component of GRF, and F_T is the tangential component of GRF. Under the assumption of negligible vertical motion, the constraints imposed on the CoP location can be equivalently interpreted as limitations on the ankle torque.

In order to assess the effectiveness of the *Ankle Strategy* for controlling external disturbances and determine the extent to which this strategy can absorb such disturbances, the stability region of the *LIPM* was derived by [9] in terms of CoM states $(x_{CoM}, \dot{x}_{CoM})$. The stability region was determined by replacing the maximum ankle torque that may be created when the CoP position is at the edge of the foot, denoted as $x_{CoP} = \delta$. Here, $\delta-$ and $\delta+$ represent the rear and front edges of the foot's support region, respectively.

$$\delta^- < \frac{\dot{x}_{CoM}}{w} + x_{CoM} < \delta^+ \tag{5}$$

Equation 5 defines the stability region condition in the CoM state space. Fig. 5 illustrates the specific region within the CoM state space where the *Ankle Strategy* effectively absorbs external perturbations. This finding also indicates that in cases where the torque exerted by the ankle is insufficient to regain balance, alternative strategies to prevent falling should be considered.

2.3 Hip Strategy

As indicated in the biomechanical studies of balance, it has been observed that utilizing the *Ankle Strategy* is appropriate mostly while encountering minor disturbances. This constraint arises due to the upper limit of ankle torque that can be exerted while ensuring that the CoP remains within the boundaries of the support polygon. Hence, to ensure stability in the presence of greater external

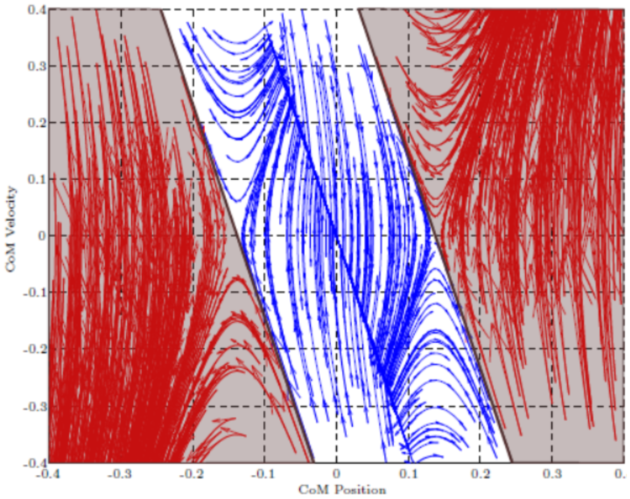

Figure 5: Stability region of the *Ankle Strategy* in terms of CoM states $(x_{CoM}, \dot{x}_{CoM})$ using *LIPM* with PD controller for the ankle torque [2]. The white area represents the stable region where the *Ankle Strategy* is deemed adequate for converging the CoM state space to the equilibrium point.

forces, an alternative balance strategy, such as the *Hip Strategy*, needs to be implemented. The *Hip Strategy* involves the combined utilization of both the ankle and hip joints, as shown in Fig. 6a. In contrast to the *Ankle Strategy*, the *Hip Strategy* presumes the presence of a flywheel attached to the CoM. This assumption enables the utilization of the *Linear Inverted Pendulum Plus Flywheel Model* for investigating this particular balance strategy.

Linear Inverted Pendulum Plus Flywheel model: The torque produced around the CoM, which is equal to the change in angular momentum, can significantly impact push recovery. The torque observed results from the rotational movement of the upper body, encompassing both the torso and arms. Therefore, in this simplified model shown in Fig. 6b, it is possible to utilize a flywheel mounted on the CoM as an approximation for the upper body. The mathematical representation of the system's behavior can be expressed as follows

$$m\ddot{x}_{CoM} = \frac{mg}{z_0}(x_{CoM} - x_{CoP}) - \frac{\tau_y}{z_0} \tag{6}$$

$$I_y\ddot{\theta}_y = \tau_y \tag{7}$$

$$\dot{x}_{CoP} = u \tag{8}$$

where τ_y is the torque about the CoM in the sagittal plane, θ_y is the angle of the flywheel and I_y is the inertia of the flywheel.

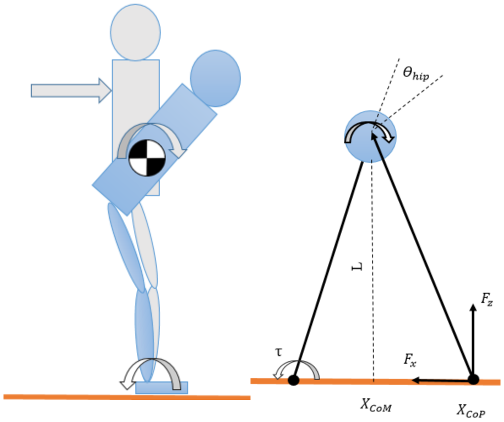

(a) (b)

Figure 6: (a) The *Hip Strategy*, (b) The *Linear Inverted Pendulum Plus Flywheel Model.*

The stability region for the *Hip Strategy* was also derived in [9]. In this strategy, both the maximum ankle torque and the maximum torque exerted by the flywheel about the CoM were essential to derive the stability region of the *Hip Strategy* as defined by equation 9.

$$\delta^- - \frac{\tau_{max}}{mg}(\exp(wT_{max}) - 1)^2 < \frac{\dot{x}_{CoM}}{w} + x_{CoM} < \delta^+ + \frac{\tau_{max}}{mg}(\exp(wT_{max}) - 1)^2 \tag{9}$$

where τ_{max} is the maxmium torque generated by the upper body (flywheel), $T_{max} = \sqrt{\frac{I\theta_{max}}{\tau_{max}}}$, I and θ_{max} are the moment of inertia and the maximum rotational angle of the flywheel, respectively.

If the condition depicted in equation 9 is satisfied, it signifies that the *Hip Strategy* can effectively manage the external disturbances. Conversely, the robot must execute a step to prevent falling if the condition is not achieved. The stability area, which illustrates the requirement as mentioned earlier, was graphed in the [2], as depicted in Fig. 7. Additional information regarding the derivation of the stability region of the *Ankle Strategy* and *Hip Strategy* can be found in [9] [2].

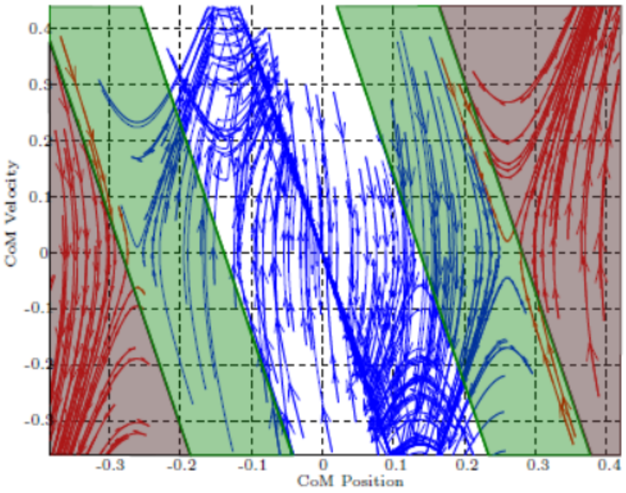

Figure 7: Stability region of the *Hip Strategy* using a *Linear Inverted Pendulum Plus Flywheel Model* with a bang-bang flywheel control [2]. In this case, the stability region is larger than the *Ankle Strategy*, indicating the ability of this strategy to maintain stability in high external disturbances. The blue trajectories are stable, while the red trajectories are unstable.

2.4 Step Strategy

According to the study of Biomechanics, when humans are unable to maintain balance using their ankle, hip or both of them, they naturally take a step in the direction of the external force exerted as shown in Fig. 8. Hence, the *Step Strategy* is used in scenarios where maintaining balance cannot be achieved through any form of body movement. It is essentially to precisely select the placement of the step in order to provide stability and avoid any violations of the kinematics and dynamics constraints of the bipedal robot. Definitely, the impact of the pushing force on the CoM will affect both the horizontal and vertical velocities of the CoM. Nevertheless, *LIPM* shown in 4b remains applicable for investigating this strategy by ignoring the vertical motion of the CoM. Using the *LIPM*, the orbital energy defined in [3] can be employed to derive the step position x_{step} necessary to stop the forward movement of the CoM. The orbital energy is conserved in the motion of *Linear Inverted Pendulum*, which means it remains constant before and after the point of impact (E_{before}=E_{after}). More information regarding the orbital energy and *LIPM* stepping can be found in [3] [9] [2]. Alternative methods are employed to determine the necessary step position for stability maintenance based on momentum knowledge.

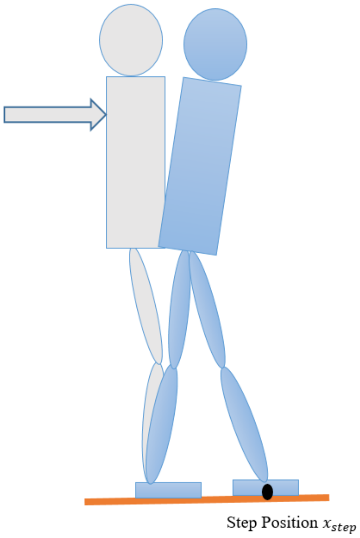

Figure 8: The *Step Strategy.*

2.5 Static and Dynamic Balance of a Biped Robot

An Industrial robot has a fixed base on the ground, which allows it to move freely within the joint moveable range. In contrast, the base of the bipedal robots (sole) are not fixed to the ground. Therefore, bipedal robots must move their joints while maintaining their balance. To comprehend the stability, it is crucial to understand the relationship between the support polygon, the CoM, and the Zero Moment Point (ZMP). The support polygon refers to the region created by enclosing all the contact points between the robot and the ground using an elastic cord braid [3], as shown in Fig. 9. Mathematically, the support polygon is formally defined as the convex hull, the minimal convex set that encompasses all contact points.

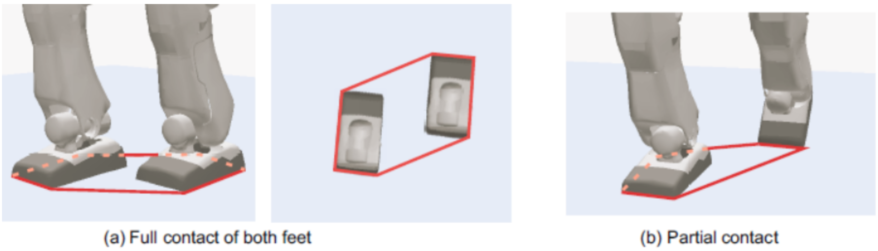
(a) Full contact of both feet

(b) Partial contact

Figure 9: Support polygon [3].

The concept of the ZMP was initially introduced by [11] as a criterion for assessing the stability of biped robots. Understanding the concept of the ZMP is crucial for the development

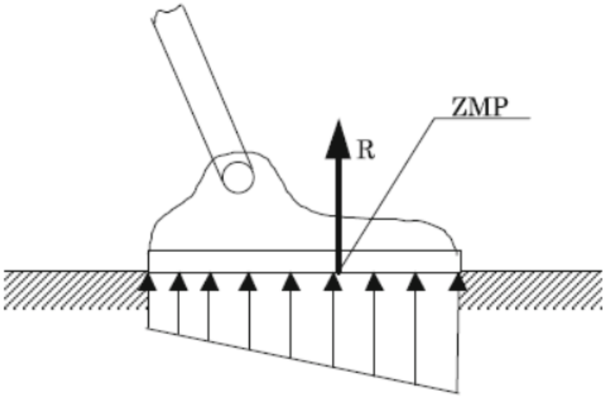

Figure 10: The Zero Moment Point (ZMP) [4].

and implementation of balance control algorithms. The ZMP refers to a specific location on the floor where the resultant moment caused by all forces operating on the robot does not possess any horizontal components [12]. The ZMP, also known as the CoP, is the position on the ground where the robot experiences the contact force. This is illustrated in Fig. 10. The ZMP/CoP value can be measured by using sensors attached to the feet or ankle joints [13], or derived from the dynamics.

To ensure the static balance of a biped robot, the CoM must be positioned within the bounds of the support polygon on the ground. Conversely, the dynamic balance is upheld when the ZMP is located within the area defined by the support polygon [14] [15]. Fig. 11 demonstrates that when a human is standing on the ground, the ZMP aligns with the projection of the CoM on the ground. In such a scenario, an individual can maintain balance if the ground projection of the CoM lies entirely within the support polygon. Conversely, when a human moves dynamically, as depicted in Fig. 11, the CoM may be located outside the support polygon on the ground. Nevertheless, the ZMP always remains within the boundaries of the support polygon.

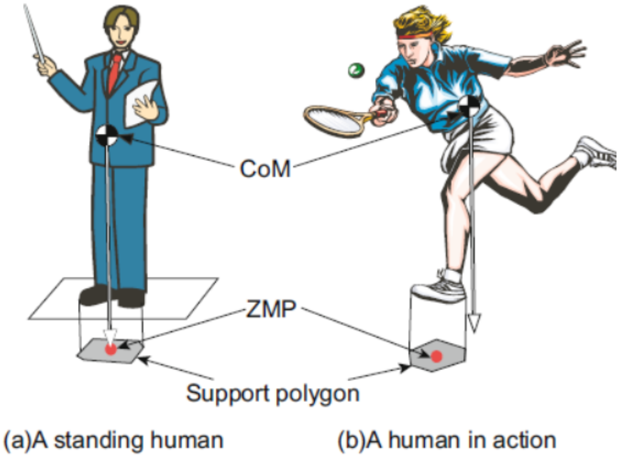

Figure 11: Static and dynamic balance [3].

2.6 Balance Control of Bipedal Robots

As mentioned in section 2.1, Human balance experiments have revealed natural responses when pushed, including the *Ankle Strategy* and *Hip Strategy*, depending upon the magnitude of the force. *Ankle Strategy* immobilizes all joints except the ankles, while the *Hip Strategy* mobilizes both the ankle and hip joints. The rotational movement of the upper body (waist) produces angular momentum, which assists in absorbing large external forces [16]. The *Ankle Strategy* was examined in [17], which focused on the fundamental dynamic equation controlling an inverted pendulum. In previous research [18], the inverted pendulum model was expanded to incorporate the robot's response to external forces using gyro sensors. The gyro sensors were employed to measure the angular velocity of the upper body movement of the robot. This data was then utilized to provide feedback for controlling the ankle joint, with the ultimate goal of achieving balance. The *Ankle Strategy* was also introduced in [19] to stabilize a humanoid robot in the sagittal and frontal planes when subjected to external pushing forces. The regulation of the ZMP or CoP position to zero was achieved by manipulating the reference position θ_d, using a joint position Proportional-Derivative (PD) controller. In [18] [19], it is assumed that the legs are massless (lightweight legs), a characteristic unusual in some legged robots. Additionally, it is observed that the *Ankle Strategy* fails to maintain stability when subjected to greater pushing forces. In [16] [20] [5], *Hip Strategy* was applied . For instance, in [16], a humanoid robot was modeled as an inverted pendulum with a flywheel attached to the CoM. To control CoM position and velocity, Virtual Model Control (VMC), analogous to PD control, was used. However, the act of locking the knee joint leads to the loss of its ability to absorb high external forces. Furthermore, its applicability depends on CoM positioning relative to the hip joint (The CoM must be exactly at the hip joint), which is only sometimes valid.

In [5], Linear Quadratic Regulator (LQR) and Computed Torque Control (CTC) were developed to calculate the desired CoP position. Then, an integral control was proposed to regulate the position of the CoP. Despite the satisfactory results, this approach was applied to a two-link robot model in an ideal simulation environment where uncertainties in dynamics are neglected. The application of this method to a bipedal humanoid robot may yield inaccurate results, as discussed later in this study.

The *Linearized Double Inverted Pendulum* (*LDIP*) model was introduced by [21] to describe the dynamics of a humanoid robot that can employ *Ankle* and *Hip* strategies. In [21], a control architecture based on Linear Quadratic Regulator (LQR) was also presented. This architecture aims to stabilize the hip joint position relative to the CoP in the horizontal direction, as well as the angular position of the torso relative to the ground normal. In addition, a constraint on ankle torque was incorporated into the LQR-based control system to ensure that the CoP remains within the support polygon. However, the hip joint position was inaccurately determined in relation to the CoP point, since it was actually determined in relation to the frame of the ankle joint. This calculation lacks precision in determining the exact position of the hip joint, leading to inefficient performance. In addition, the LQR weight matrices Q and R were adjusted manually in [21] to achieve the appropriate response. However, this approach may pose challenges when attempting to determine global weight matrices for different values and locations of pushing forces.

On the other side, numerous researchers emphasize the significance of regulating the rate of change of momenta in order to preserve stability (*momentum-based balance control strategies*). In the past, the predominant focus of balance control approaches involved regulating a robot's linear momentum or CoM movement to maintain balance. Subsequently, Popovic and his colleagues in [22] highlighted the importance of effectively controlling angular momentum to balance. The findings of [22] revealed that the central nervous system plays a crucial role in regulating the angular momentum during human walking. A nonlinear relationship was also observed between the F_{GRF}, CoM position, and CoP position. Hence, to achieve complete control over the CoP, it is necessary to effectively regulate both angular and linear momenta [23–26].

The equation of motion for the humanoid robot was expressed in relation to the combined linear and angular momentum, as stated in [23]. The total momentum is a six-dimensional vector that characterizes the macroscopic behavior of the complete robot. The desired linear and angular momenta were first defined, and then the joint velocities corresponding to these desired momenta were computed using the centroidal momentum dynamics. However, the robot's ability to maintain balance was not considered, so it may become unstable when the desired input momenta values are high. Therefore, in [6], the authors established the required rate of change of angular momentum by defining it concerning the position of the CoP. The desired changes in momentum were successfully accomplished in [25] [27] via a multi-objective optimization technique. This involved the precise selection of joint accelerations and the subsequent computations of matching torques using inverse dynamics. The multi-objective optimization problem described in [25] included three components, with one component aimed at minimizing the discrepancy between the desired and actual rate of change of linear momentum. The second term aimed to minimize the discrepancy in the rate of change of angular momentum, which was defined in terms of the position and velocity of the CoP. The third term was to achieve the character's upright stance through tracking. The results indicated that the character is capable of maintaining balance when subjected to external perturbations during both the single and double stance phases.

In [26], the author introduced a model-based approach, known as Dynamic Balance Force Control (DBFC), to calculate the whole body joint torques. This calculation is based on the motion of the CoM and the forces experienced at the points of contact. The contact forces that control the rate of change of linear and angular momenta were established via a constrained optimization process. However, the balancing stability problem did not incorporate the contribution of angular momentum, as it was assumed that the desired rate of change of angular momentum is zero. The method proposed in [28] involved the regulation of the CoM through the modulation of angular momentum, particularly in situations where significant external perturbations are present. In [28], when it was impossible to achieve both momenta, more weight was placed on the linear momentum.

In [6], balance control objectives were defined in terms of CoM and CoP values, focusing on controlling the rate of change of momenta using a three-link planar model. Two primary balance phases were identified: the *Reflex Phase*, rapidly responding to external forces to stabilize the rate of change of momenta using simple Proportional (P) controller, where the difference between the desired and actual linear momentum represents the error, and the *Recovery Phase*, which aimed to reposition the body when disturbance forces subsided, with a control law designed to maximize potential energy.

In our study, we enhance the approach of *momentum-based balance control* by replacing the simple linear controller with an improved reaching law-based SMC for linear momentum stabilization, as will explained in section 4.2.1. Furthermore, we define the desired rate of change of angular momentum about the CoM, accounting for the desired rate of change of linear momentum (section 4.2.2). Unlike prior works, where the two-phase controllers were applied sequentially, we propose a null-space-based method to restore the robot's upright posture during recovery without interfering with primary momentum controllers (section 4.3).

2.7 Summary

Section 2 initially emphasized the biomechanical studies related to human balance. Subsequently, the *Ankle* and *Hip Strategies* were analyzed using simplified models specifically designed to investigate these strategies. The stability regions of the *Ankle* and *Hip Strategies*, as determined by terms of CoM states, have been demonstrated. The *Step Strategy* was also analyzed as a method used when no form of bodily movement can attain balance. Section 2.5 showed the relationship between the CoM, ZMP and the support polygon (static and dynamic balance).

Section 2.6 surveyed the strategies used to control balance in bipedal robots. It reviewed prior research that focused on utilizing of *Ankle/Hip Strategy* to stabilize the ZMP or CoP. However, these human-inspired techniques have limitations when it comes to maintaining stability. The literature review also highlighted the significance of stabilizing the rate of change of momenta by utilizing (*Momentum-Based Strategy*). These strategies focused on optimizing either the GRF or joint accelerations to accomplish the required momenta change rate.

3 HURON Lower Body System

HURON is a full-sized humanoid robot built from the ground up by our team at Worcester Polytechnic Institute (WPI). This section will describe the mechanical, electrical, and software details of the lower body of HURON.

3.1 Mechanics

HURON is designed with human anatomy in mind, with two lower limbs, including hips, thighs, crura, and feet. The robot is mainly built with 6061 aluminum and low-carbon steel. It weighs about 44 kg, stands 1.4 m tall, and provides 12 Degrees of Freedom (DoF) when both feet are flat on the ground — six on each limb, including hip joint roll, pitch, yaw, knee joint pitch, and ankle joint roll and pitch. All 12 joints in the lower body of HURON are revolute joints equipped with BLDC motors. Each hip and knee joint includes a two-stage 40:1 planetary gearbox and a 2:1 belt drive, which totals an 80:1 reduction. The ankle joints include SHD-25-160-2SH harmonic drive gears with a 160:1 gear ratio, which permits high torque and high-speed applications like walking.

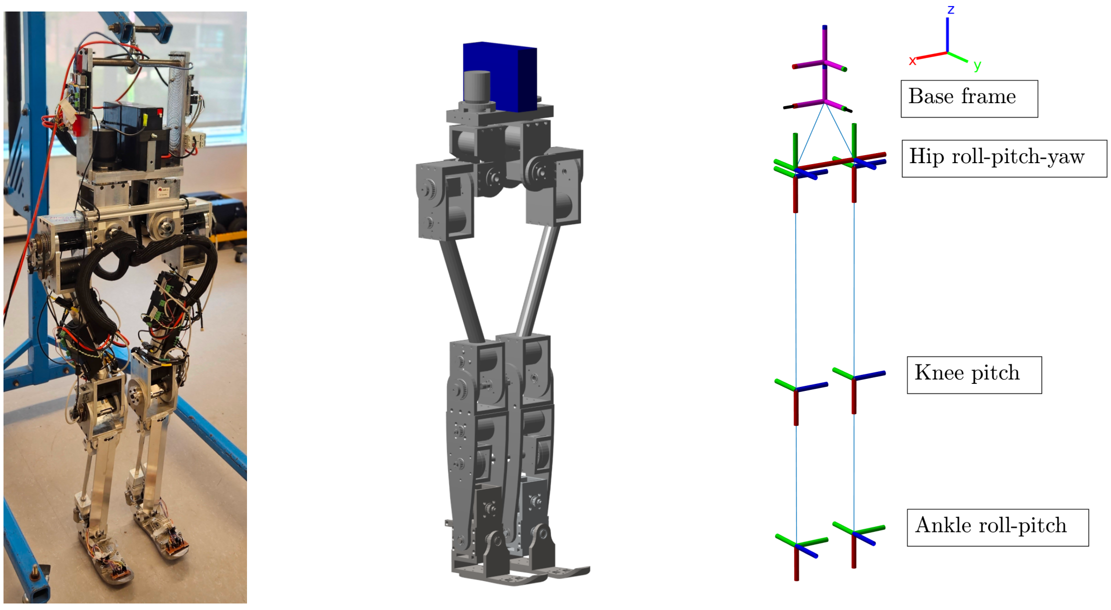

(a) (b) (c)

Figure 12: HURON lower body. (a) physical robot, (b) simulation model, (c) robot frames.

The mechanical properties of HURON are described in Fig. 13 and Tables 1 and2.

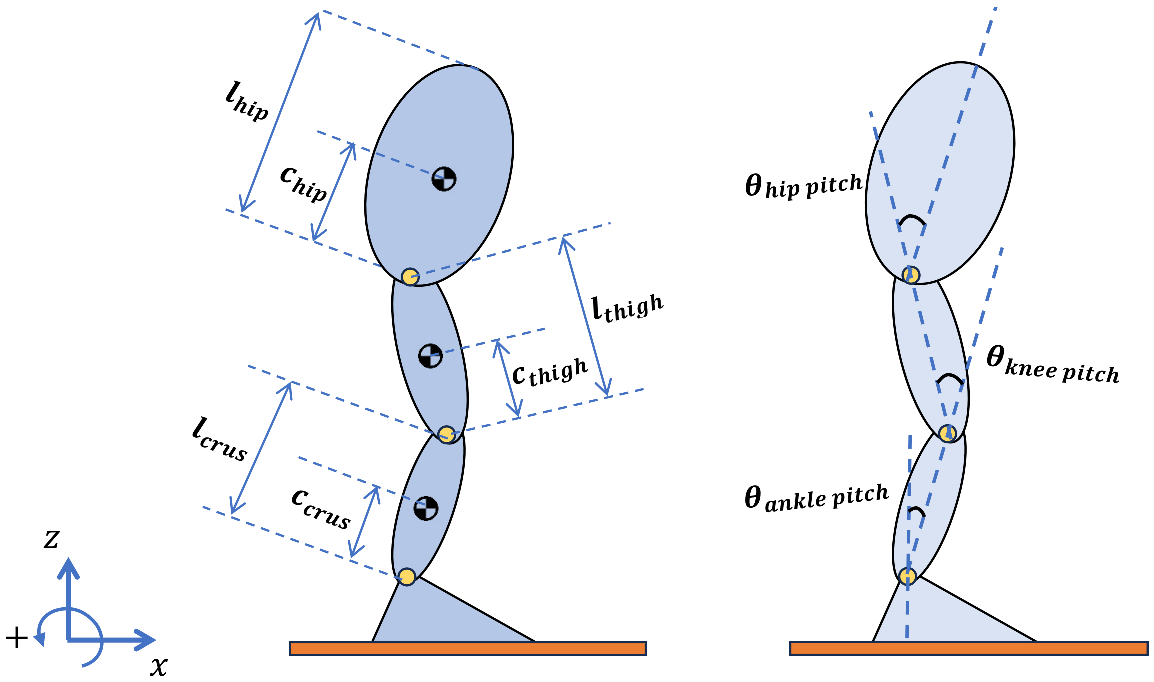

Figure 13: Robot properties from the side view. (a) link lengths and positions of the links' CoM, (b) joint pitch angles.

Table 1: Robot link properties summary.

Link name	**Length l_i [mm]**	**CoM offset c_i [mm]**	**Mass m_i [kg]**
Hip	326.62	158.5	10.19
Thigh	496.28	245.17	4.26
Crus	370	151.49	5.91

Table 2: Robot joint properties.

Joint name	**Range of motion [rad]**
Hip roll	-0.01 to 0.5236
Hip pitch	-1.2217 to 1.2217
Hip yaw	$-\pi$ to π
Knee pitch	$-\frac{\pi}{2}$ to $\frac{\pi}{2}$
Ankle roll	-0.3491 to 0.3491
Ankle pitch	-0.5236 to 0.1745

3.2 Electronics

The main electrical components of HURON include a Raspberry Pi as the central processing computer, ODrive motor controllers, and a foot force sensor system managed by an Arduino Mega. The overview electronics system of the robot is shown in the diagram below.

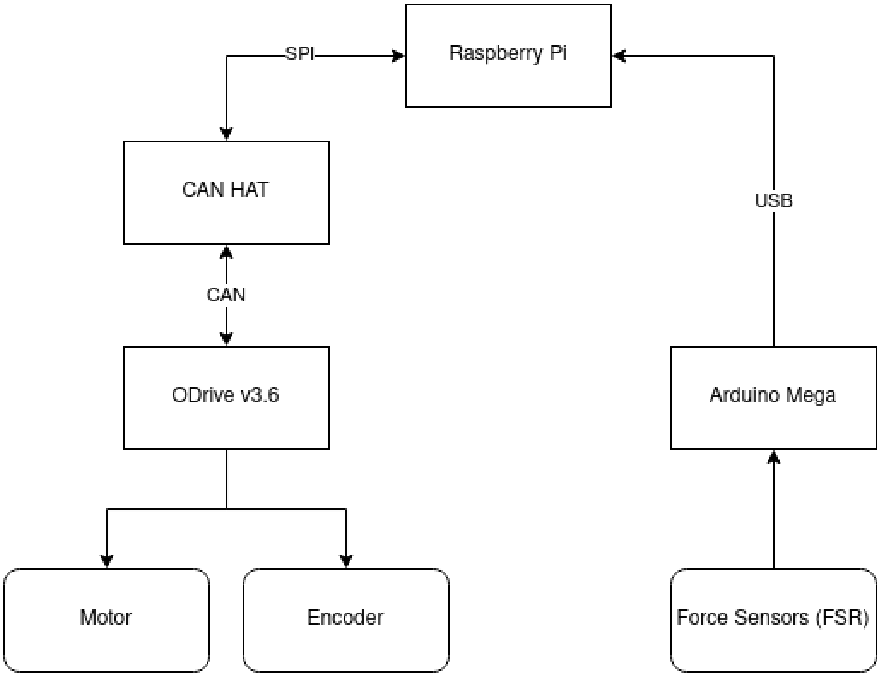

Figure 14: Electronics system of HURON.

3.2.1 Microcontrollers

HURON's main processing unit is a Raspberry Pi 3B Rev 1.2. The Raspberry Pi runs the main code, which includes high-level application and control code of lower-level components. The Raspberry Pi is installed with Ubuntu 20.04.

For the foot sensor system, we use an Arduino Mega 2560 for reading Force Sensing Resistors (FSRs), calculating the CoP, and sending the results to the Raspberry Pi for higher-level processing.

3.2.2 Motors and motor controllers

The revolute joints of HURON are actuated by the 6374 190KV 3500W BLDC motors from Flipsky. We use ODrive v3.6 motor controllers to operate these BLDC motors. Each motor controller can control two motors. The ODrive communicates via Controller Area Network (CAN) protocol with the Raspberry Pi, which uses a CAN HAT with SPI. The ODrive allows sending position, velocity, and torque commands. It also allows various configurations, such as current limit, velocity limit, torque constant, and more.

3.2.3 Sensors

HURON is equipped with AMT102-V rotary encoders. The encoders are connected to ODrive; after being processed by ODrive, the encoder data (position and velocity) are transmitted back to the Raspberry Pi.

To measure the Ground Reaction Forces (GRFs), which are necessary for determining the stability of the robot, we created a sensor system on the feet. Each foot has four FSR connected to the ground via four small rubber pads. The sensor outputs go through our custom-made amplifier circuit and are used by the Arduino Mega to calculate the stability indicators like CoP. For the simulation model of HURON, we used Force/Torque sensors attached to the ankle joints to calculate the position of the CoP, as explained in appendix C.

3.3 Software

We developed our own modular and flexible software framework that contains several abstraction layers. The framework aims to assist researchers who wants to focus on high-level algorithms like walking or other advanced actions. This is done by hiding the low-level implementation details as much as possible. The framework also simplifies the sim-to-real problem by providing a unified API for simulation and real robot code, which also allows for adding third-party extensions like dynamics or control libraries.

3.4 Simulation Model of HURON in Gazebo

Gazebo is an open-source 3D robotics simulator. Gazebo incorporated the Open Dynamics Engine (ODE) physics engine, OpenGL graphics, and support code for simulating sensors and controlling actuators. The ODE is a physics engine implemented and written in C/C++. It consists of two primary elements: a simulation engine for rigid body dynamics and an engine for detecting collisions.The ankle joints were equipped with force/Torque sensors to measure the ground response forces, which would be utilized for determining the position of the Center of Pressure (CoP). Furthermore, HURON model was switched from a position-controlled implementation to an effort-controlled implementation in Gazebo in order to validate the effectiveness of the proposed push recovery control system, which will be presented in section 4.

3.5 Summary

This section provided a comprehensive description of HURON's lower body, including its mechanical, electrical, and software components.

4 The Push Recovery Control: Standing Stability

In this section, we will introduce our proposed push recovery control system that is based on momentum.

4.1 Mechanics of Balance

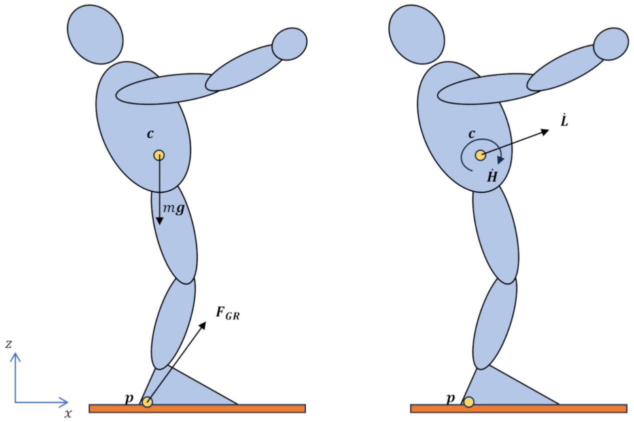

Figure 15: External forces acting on a human body and the equivalent rate of change of linear and angular momenta.

The conservation law of linear and angular momenta, denoted by L and H, holds without an external force. Newton's laws state that forces and torques exerted on a body are equal to the momenta changes. Without external disturbances, a standing bipedal robot's momentum is exclusively caused by the Ground Reaction Force F_{GR} and the gravitational force. Derivatives of linear and angular momentum are

$$\dot{L} = \sum F = mg + F_{GR} \tag{10}$$

$$\dot{H} = \sum \tau = (p - c) \times F_{GR} \tag{11}$$

where m is the total mass of the robot, g is the gravitational acceleration, F_{GR} is $[F_{GR,x}, F_{GR,y}, F_{GR,z}]^\top$, which is applied to the center of the pressure point, p is the CoP location $[px, py, 0]^\top$, c is the

CoM of the robot $[cx, cy, cz]^\top$ (see Fig. 15). The laws of Newton also state that $L = m\dot{c}$ and $\dot{L} = m\ddot{c}$. Controlling the robot's CoM acceleration is similar to controlling its rate of change of linear momentum. Furthermore, in the absence of pushing force, equation (10) demonstrates that the F_{GR} is regulated by controlling the linear momentum. The angular momentum is shown to be related to the CoP and F_{GR} by equation (11). A typical balance approach is to maintain the CoM projection within the boundaries of the support polygon. However, controlling the CoP is also essential since losing CoP control can cause the robot to topple over due to rotation via angular momentum. The CoP must remain within the convex hull of the ground support area.

If equation (10) and equation (11) are applied to our bipedal robot (HURON) in the sagittal plane and with a horizontal pushing force $F_{pushing}$ as depicted in Fig. 16, we obtain the following equations:

$$\begin{aligned} \dot{H}_{CoM,y} &= \sum \tau_{CoM,y} \\ &= (p_x - c_x)F_{GR,z} - c_z F_{GR,x} - u_z F_{pushing} \end{aligned} \tag{12}$$

where u_z is the location of the pushing force with respect to CoM.

$$\sum F_x = -F_{GR,x} = m\ddot{c}_x = \dot{L}_x \tag{13}$$

$$\sum F_z = F_{GR,z} = \dot{L}_z + mg \tag{14}$$

Plug equation (13) & (14) into equation (12) and solving for p_x, we obtain

$$p_x = c_x + \frac{\dot{H}_{CoM,y} - c_z \dot{L}_x}{\dot{L}_z + mg} + \frac{u_z F_{pushing}}{\dot{L}_z + mg} \tag{15}$$

Equation (15) illustrates that in static conditions, the CoP (p_x) and the CoM (c_x) are both located initially at the same point on the horizontal plane. A positive pushing force will cause p_x to move forward. As the force increases, the CoP moves toward the edge of the foot. To prevent the robot from falling in the clockwise direction, a negative $\dot{H}_{CoM,y}$ must be applied about the CoM [6]. If the robot stays rigid or accelerates backward in response to the force, p_x will be pushed closer to the edge of the support polygon. Therefore, this study proposes a balanced approach to

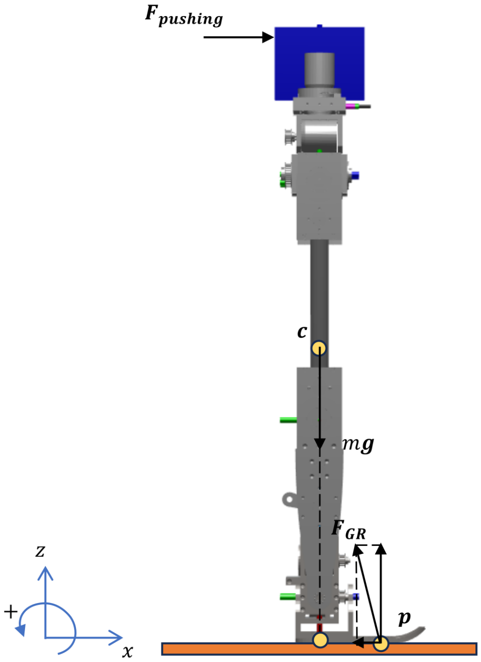

Figure 16: A disturbing force applied to the robot.

regulating both CoM and CoP by regulating linear and angular momenta.

4.2 Disturbance Absorption Phase

The objective of this phase is to generate $\dot{H}_{CoM,y}$ to absorb the disturbance while regulating the CoM via the proposed reaching law-based Sliding Mode Control (SMC).

4.2.1 Linear Momentum Controller

According to Newton's laws, controlling the robot's CoM is the same as controlling its rate of change of linear momentum. As a result, to ensure CoM stability, this study proposes an improved reaching law for SMC. Reaching and sliding are the two main parts of the SMC [29]. SMC is based on the design of a switching surface and the synthesis of a controller to drive closed-loop state trajectories to the sliding mode surface $s = 0$ in finite time. s represents the system state and is formed of trajectory errors. The sliding phase reaching condition is usually expressed as $s\dot{s} \leq 0$. A conventional switching function s is given by,

$$s = \dot{e} + \lambda e \tag{16}$$

where λ is a nonzero constant, which determines the chattering level and reaching time, e, $\dot{e}$ are the error in CoM position and velocity respectively and they are defined as follows:

$$e = c_x - c_{x,r} \tag{17}$$

where $c_{x,\ r}$ is the reference CoM position

$$\dot{e} = \dot{c}_x - \dot{c}_{x,r} \tag{18}$$

where $\dot{c}_{x,r}$ is the reference CoM velocity.

The torques τ in equation (55) should be designed to derive the system to the equilibrium point, and the sliding condition $s\dot{s} \leq 0$ should be satisfied $\forall t$. The sliding condition indicated above can be satisfied by developing a reliable reaching law, which is the differential expression of s. Nevertheless, it is crucial to acknowledge that the SMC does have its limitations. The occurrence of an undesired behavior known as chattering arises due to the non-instantaneous transition between the reaching and sliding phases. The act of chattering has the potential to generate high-frequency, substantial disruptive dynamics. Thus, several studies [30–34] have been undertaken to examine the SMC with reaching laws, which was initially proposed by Gao and Hung [35]. The reaching law-based SMC proposed by Gao and Hung [35] includes different types: the Exponential Reaching Law (ERL), the Constant Power Reaching Law (CPRL), and the Constant Reaching Law (CRL).

In [31], the authors proposed a new approach called the Enhanced Exponential Reaching Law (EERL) that integrates the concepts of the Exponential Reaching Law and the Constant Reaching Law to mitigate chattering effects and enhance the tracking performance. [32] introduced a Power Reaching Law (PRL) that has the ability to adjust the parameters by switching between two power values depending on the value of s. [33] employed the Double-Power Reaching Law in the sliding mode control approach to achieve asymptotic tracking of the desired position and velocity.

This method effectively addresses the issue of excessive chattering commonly associated with the conventional sliding mode control reaching law. However, the convergence time is slow.

The Constant Rate Reaching Law can be mathematically represented as:

$$\dot{s} = -k\ sgn(s) \tag{19}$$

where k is a positive constant gain. If the increase in the k parameter in the Constant Rate Reaching Law is leading to chattering, it is likely because a higher k value leads to a more aggressive control action.

Gao and Hung [35] also proposed the Constant Power Rate Reaching Law, which can be expressed as follows:

$$\dot{s} = -k|s|^{\rho} sgn(s) \tag{20}$$

where k and ρ are constant and positive parameters.

The reduction of the parameter ρ has the potential to mitigate chattering phenomena; nevertheless, it is necessary to note that this adjustment may result in an increase in the time required to accomplish the desired outcome. Therefore, to mitigate the chattering phenomenon and simultaneously enhance the rate at which the sliding mode is approached, this study proposes the improved reaching law-based SMC designed to regulate the linear momentum or CoM motion.

The proposed reaching law for SMC is the **Variable Power Rate Reaching Law ($\dot{s}$)**, which utilizes a **variable power** function, denoted as $(\delta\,(s))$. The **variable power** is a function that increases exponentially with the system state s.

The **Variable Power Rate Reaching Law** is

$$\dot{s} = -k_1|s|^{\delta} sgn(s) \tag{21}$$

where the **variable power** $(\delta\,(s))$ is

$$\delta\,(s) = k_3\left(1 - e^{-\sigma|s|^{\eta}}\right),\ \ \delta\,(s) \in [0, k_3] \tag{22}$$

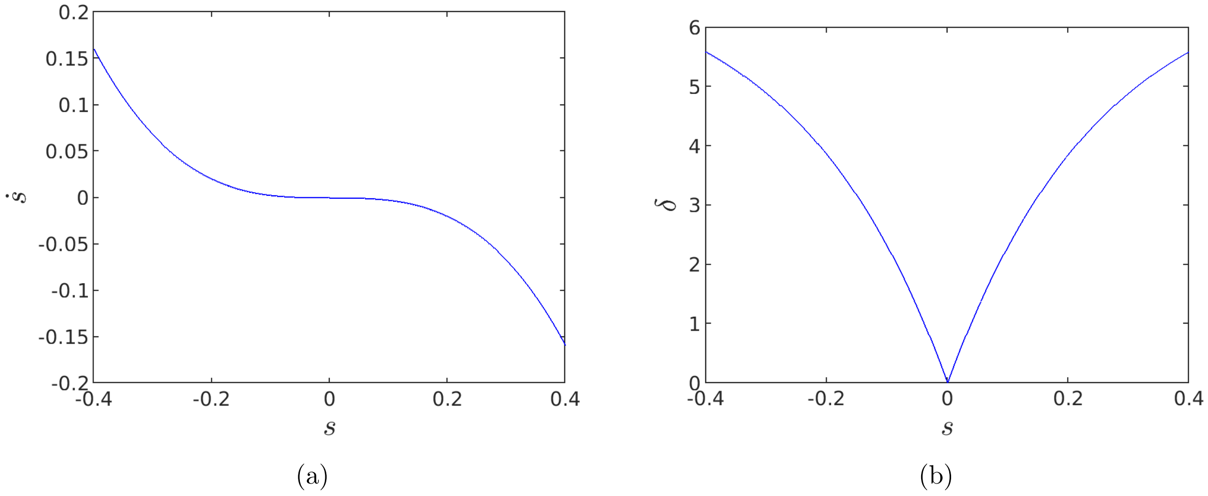

Figure 17: (a) Reaching law $\dot{s}$ versus system state s, (b) δ versus system state s.

and k_1, k_3, σ, η are strictly positive parameters. Analyzing the **Variable Power Rate Reaching Law ($\dot{s}$)** presented in equation (21) reveals that the controller can adapt dynamically to changes in the switching function, as shown in Fig. 17a. As $|s|$ grows, the **variable power** $\delta(s)$ tends toward k_3, implying that the further the sliding mode state s is to the equilibrium state, the more quickly it approaches, as shown in Fig. 17b. If $|s|$ goes down, the **Variable Power Rate Reaching Law ($\dot{s}$)** gets closer to zero at a slower rate as the **variable power** $\delta(s)$ approaches a small value close to 0. This behavior indicates that the **variable power** $\delta(s)$ decreases as s approaches the equilibrium state, and chatter hardly occurs. Therefore, the proposed reaching law can not only eliminate chattering but also have fast convergence and make the system from any point to approach the sliding mode surface in finite time, regardless of how far away or how close it is to the surface.

Theorem 1. The stability condition holds for the reaching law given by equation (21).

Proof. A Lyapunov function is considered:

$$V = \frac{1}{2}s^2 \tag{23}$$

Combining with equation (21), the time derivative of V is given by

$$\dot{V} = s\dot{s} = -k_1|s|^{\delta}sgn(s)s \tag{24}$$

$$\dot{V} = s\dot{s} = -k_1|s|^{\delta+1} \tag{25}$$

where $k_1 > 0$, and then $\dot{V} < 0$, and the stability condition is satisfied. The system state s can reach the equilibrium point $s = 0$.

Theorem 2. For reaching law (21), the system states s and $\dot{s}$ can converge to the equilibrium zero in a finite amount of time; that is, $s = \dot{s} = 0$ after a finite amount of time.

Proof. Suppose $s\left(0\right) = s_0 > 0$

$$\dot{s} = \frac{ds}{dt} = -k_1|s|^{\delta}sgn(s) \tag{26}$$

$$\frac{1}{-k_1|s|^{\delta}sgn(s)} = F(s) \tag{27}$$

$$\int_{s_0}^{0} F\left(s\right)ds = \int_{0}^{t_r} dt \tag{28}$$

Using the Double-Exponential (DE) transformation and the trapezoidal rule, we perform a numerical integration to determine the time required to reach the sliding surface $s = 0$. The DE transformation was first proposed by Takahasi and Mori in 1974, in order to compute the integrals with end-point singularity [36]. In DE transformation, $s = M\phi(t)$ where M is constant, $\phi(t)$ is an analytic function over $(-\infty, +\infty)$. If we apply DE transformation to equation (27), we obtain

$$t_r = M\int_{-\infty}^{+\infty} F(M\phi(t))\phi(t)dt \tag{29}$$

where $\dot{\phi}(t)$ is the time derivative of $\phi(t)$. Significantly, the integrand's decay should be double exponential following the transformation, therefore $\phi(t)$ should be chosen accordingly.

$$|F(M\phi(t))\dot{\phi}(t)| \approx e^{(-ce^{t})}, |t| \to \infty \tag{30}$$

The authors of [37] proposed a robust DE transformation with a function $\phi(t)$ satisfying the above condition as follows:

$$\phi(t) = \frac{t}{(1 - e^{-2t-\alpha(1-e^{-t})-\beta(e^{t}-1)})} \tag{31}$$

$$\beta = \frac{1}{4}, \alpha = \frac{\beta}{\sqrt{1 + M \log{(1 + M)} (4\pi)}} \tag{32}$$

Then, the trapezoidal rule with equal mesh size h is applied [36], where M and h are chosen to satisfy $Mh = \pi$.

$$t_r = Mh \sum_{k=-\infty}^{\infty} F\left(M\phi\left(kh\right)\right)\dot{\phi}\left(kh\right) \tag{33}$$

In actual computation of equation (33), the infinite summation is truncated at $k = -N_-$ and $k = N_+$ and obtain

$$t_r^N = Mh \sum_{k=-N_-}^{N_+} F\left(M\phi\left(kh\right)\right)\dot{\phi}\left(kh\right),\ N = N_+ + N_- + 1 \tag{34}$$

where N is the number of function evaluations.

The above integral is implemented in MATLAB and the results indicate that the reaching time t_r is finite, regardless the initial state value of $s_0 > 0$. When the initial state of the system is $s_0 < 0$, the proof is the same as the above one, which we can conclude that the system reaches $s = 0$ in a finite amount of time, regardless of the initial state of the system s_0.

Since this study focuses on sagittal pushes, where the robot is standing and pushed from the front or back in the sagittal plane, the lower body of HURON is simplified as a triple-inverted pendulum model ($n = 3$). The joint space accelerations $\ddot{q}$ that achieve the linear momentum controller indicated above are calculated as follows:

$$\dot{c}_x = J_x\dot{q} \tag{35}$$

where $J_x \in \mathbb{R}^{1\times n}$ is the Jacobian matrix that relates the linear velocity of CoM in x-axis with joint velocities $\dot{q}$. Take time derivative of equation (35), we obtain:

$$\ddot{c_x} = J_x\ddot{q} + \dot{J}_x\dot{q} \tag{36}$$

Time derivative of the conventional sliding surface is

$$\dot{s} = \ddot{e} + \lambda \dot{e} \tag{37}$$

where $\ddot{e} = \ddot{c}_x - \ddot{c}_{x,r}$ and $\ddot{c}_{x,r} = 0$.

Plug equations (21) & (36) into equation (37), we obtain

$$-k_1 |s|^{\delta} sgn(s) - \lambda \dot{e} = J_x \ddot{q} + \dot{J}_x \dot{q} \tag{38}$$

The controller previously presented is sufficient to regulate linear momentum or CoM motion. However, in balance dynamics, we noticed that angular momentum also contributes to balancing the bipedal robots in the presence of disturbances. As a result, the following section describes how we develop the angular momentum controller.

4.2.2 Angular Momentum Controller

Equation (15) explains that the CoP moves forward in the presence of a positive pushing force, shifting further to the foot as the pushing force increases. It is also evident that applying negative $\dot{H}_{CoM,y}$ would prevent the foot from falling forward in a clockwise direction. Therefore, in this section, we generate a clockwise $\dot{H}_{CoM,y}$ to regulate the CoP. The angular momentum about the CoM is given in [23].

$$H_{CoM,y} = A(q)\dot{q} \tag{39}$$

where $H_{CoM,y}$ is angular momentum of the robot about the CoM around y-axis, $A(q)$ is $3 \times n$ matrix and function of q. Since only the angular momentum about the y-axis is computed, $A(q)$ is reduced to $1 \times n$, and its derivative can be found in the Appendix B. Take time derivative of equation (39), we obtain

$$\dot{H}_{CoM,y} = \dot{A}\dot{q} + A\ddot{q} \tag{40}$$

The desired $\dot{H}_{CoM,y}$ is defined through two approaches:

First Approach: It is evident in the mechanics of balance that the absence of intersection between the CoP and CoM results in the generation of angular momentum around the CoM. Hence, the desired rate of change of angular momentum is expressed as

$$\dot{H}_{CoM,y} = -k_H \left(p_x - c_x\right) \tag{41}$$

where k_H is a positive tuning parameter.

Second Approach: In this approach, the third term of equation (12) is eliminated under the assumption that both the magnitude and position of the applied force are unknown. In addition, the $F_{GR,x}$ is substituted by the linear momentum controller proposed in this paper. The negative sign is added in order to create a negative $\dot{H}_{CoM,y}$, thereby aligning it with the direction of the applied pushing force. The desired $\dot{H}_{CoM,y}$ is defined as follows:

$$\dot{H}_{CoM,y} = -k_H[(p_x - c_x)F_{GR,z} - c_z(-m(\dot{s} - \lambda\dot{e}))] \tag{42}$$

It is noteworthy to state that the measurement of the (F_{GR}) in our bipedal robot HURON's simulation model is conducted through the use of Force/Torque (F/T) sensors that are affixed to the ankle joints. Consequently, the calculation of the CoP position is derived as outlined in Appendix C. However, in the real HURON model, high-quality four force sensors are employed for each foot in order to accurately estimate the present position of the CoP.

The two approaches are examined and discussed in the results section.

4.2.3 Combination of Momentum Controllers

The objective in this phase is to generate $\dot{H}_{CoM,y}$ to absorb the pushing force while regulating the CoM via the proposed SMC. By solving equation (38) and equation (40) simultaneously with the Moore-Penrose pseudo-inverse, we obtain the joint accelerations $\ddot{q}$ that satisfy the linear and angular momentum controllers as

$$\ddot{q}_{momentum} = \begin{bmatrix} J_x \\ A \end{bmatrix}^{\dagger} \begin{bmatrix} -k_1|s|^{\delta} sgn(s) - \lambda\dot{e} - \dot{J}_x\dot{q} \\ \dot{H}_{CoM,y} - \dot{A}\dot{q} \end{bmatrix}. \tag{43}$$

4.3 Posture Recovery Phase

To complete the push recovery process, an additional “posture task” is needed to bring the robot back to an upright posture. As noted by [6], the posture task may conflict with the momentum control task. Therefore, a method of combining them while minimizing conflict is necessary. For a redundant robot, this goal can be achieved by solving the redundancy resolution problem, where the additional Degrees of Freedom (DoF) can be exploited to adjust the behavior of the robot without affecting the main task, such as satisfying additional constraints or accomplishing other tasks.

Many researches have been relying on the use of null space projection method to resolve redundancy. The principle is to projecting **Lower Priority** tasks inside the null space of **Higher Priority** tasks, so that the **Lower Priority** tasks will not affect the **Higher Priority** tasks. Generalized frameworks for managing tasks with prioritization have been developed at different levels: velocity [38–41], acceleration [41], [39], [5], and torque [42–45]. The characteristics of these different approaches were discussed in [46]. Our goal with this method is to execute both the momentum task (**Higher Priority**) and the posture recovery task (**Lower Priority**) at the same time with minimal conflicts. For our push recovery application, the task dimension (two) is less than the number of joints (three), which suggests that task redundancy is available and this method can be used for an additional posture task to bring the joints back to a desired configuration. Specifically, the home configuration (upright posture) is desired after push recovery.

The posture recovery task is developed as follows:

For an n-DoF robot with a task $x \in \mathbb{R}^m$, the task is a function of joint configuration:

$$x = f(q) \tag{44}$$

Taking the time derivative of equation (44), we achieve the kinematic relationship between task velocities $\dot{x}$ and joint velocities $\dot{q}$:

$$\dot{x} = J\left(q\right)\dot{q} \tag{45}$$

where $\dot{(*)}$ denotes the time derivative of a matrix $(*)$, and $J \in \mathbb{R}^{m\times n}$ is the task Jacobian matrix.

For a redundant system, $m < n$. The general solution to equation (45) is then:

$$\dot{q}_r = J^{\dagger}\dot{x} + \left(I - J^{\dagger}J\right)\xi \tag{46}$$

where $J^{\dagger}$ denotes the Moore-Penrose inverse of the Jacobian J, $I \in \mathbb{R}^{n\times n}$ is the identity matrix, and $\xi \in \mathbb{R}^n$ is an arbitrary null space velocity vector. The null space projector $(I - J^{\dagger}J)$ ensures that ξ lies in the null space of the main task Jacobian J, thus does not affect the main task $\dot{x}$.

The null space velocity ξ can be used to specify a local optimization task, often in the form:

$$\xi = \alpha\nabla w \tag{47}$$

where $\alpha \in \mathbb{R}$ is a scalar, and $\nabla w = \frac{\partial w}{\partial q}$ is the gradient of an objective function $w(q)$. For example, to make the joints converge to a desired configuration q_d, the following cost function can be used:

$$w\left(q\right) = \frac{1}{2}\left(q - q_d\right)^T K_w(q - q_d) \tag{48}$$

where K_w is a $n \times n$ diagonal positive definite gain weighting matrix. This cost function was used in [46] and proved to be effective to generate natural human-like motion in [47].

In the acceleration level, the second-order differential equation gives the acceleration relationship:

$$\ddot{x} = \dot{J}\dot{q} \ + J\ddot{q} \tag{49}$$

Solving the inverse problem for control joint acceleration $\ddot{q}_c \in \mathbb{R}^n$, with reference task acceleration $\ddot{x}_r \in \mathbb{R}^m$:

$$\ddot{q}_c = J^{\dagger}\left(\ddot{x}_r - \dot{J}\dot{q}\right) + \left(I - J^{\dagger}J\right)\phi_N \tag{50}$$

where $\phi_N \in \mathbb{R}^n$ is an arbitrary null space joint acceleration. As shown in [46], this controller provides tracking in the task space, and together with the following formulation of desired null space acceleration, the whole controller was realized:

$$\phi_N = -K_{q,d}\dot{q} - \alpha\nabla w \tag{51}$$

in which $K_{q,d}$ is positive definite damping gain matrix.

The choice of ϕ_N in [46] is similar to a PD controller, which can be ineffective when the system has large operating region and steady state error, as is the case with our robot (HURON). Therefore, to improve the posture correction task, we implemented a SMC with Constant Power Reaching Law (CPRL) for ϕ_N:

$$\phi_N = -K_q * |s_q|^{\epsilon} sgn\left(s_q\right) - \left(\lambda_q \dot{e}_q\right) \tag{52}$$

where K_q, ϵ, $\lambda_q > 0$

$$s_q = \dot{e}_q + \lambda_q e_q \tag{53}$$

where e_q is the error in joint angular position.

Equation (50) consists of two component control accelerations:

The first term is the **Higher Priority** task, which in our case is the acceleration of the momentum controller ($\ddot{q}_{momentum}$) as defined in equation (43).

The second term is the **Lower Priority** task, which in our case is the acceleration of the posture controller ($\ddot{q}_{posture}$)

$$\ddot{q}_{posture} = \left(I - J^{\dagger} J\right) \phi_N \tag{54}$$

where, specifically in our case, $J = \begin{bmatrix} J_x \\ A \end{bmatrix} \in \mathbb{R}^{2\times3}$ is the momentum task (main task) Jacobian, I is the identity matrix, and ϕ_N is defined in equation (52).

The joint space equation of motion for a rigid-body, n DoF robot is:

$$\tau = M\left(q\right)\ddot{q} + C\left(q, \dot{q}\right)\dot{q} + G\left(q\right) \tag{55}$$

where q, $\dot{q}$, $\ddot{q} \in \mathbb{R}^n$ are joint positions, velocities, and accelerations, respectively, $\tau \in \mathbb{R}^n$ are torques applied at the joints, $M\left(q\right) \in \mathbb{R}^{n\times n}$ is the mass matrix, $C\left(q, \dot{q}\right) \in \mathbb{R}^{n\times n}$ is the Coriolis and centripetal matrix, and $G\left(q\right) \in \mathbb{R}^n$ is the gravitational vector.

The momentum torque is then calculated as follows:

$$\tau_{momentum} = M\left(q\right)\ddot{q}_{momentum} + \boldsymbol{C}\left(q, \dot{q}\right)\dot{q} + G(q) \tag{56}$$

The posture torque can be calculated by:

$$\tau_{posture} = M\left(q\right)\ddot{q}_{posture} \tag{57}$$

The final control law is computed by adding the momentum and posture torques:

$$\tau_c = \tau_{momentum} + \tau_{posture} \tag{58}$$

where $\tau_c \in \mathbb{R}^n$ is the control torque input.

Fig. 18 illustrates the proposed push recovery control, which comprises momenta controllers for mitigating external disturbances and posture recovery systems for maintaining an upright posture.

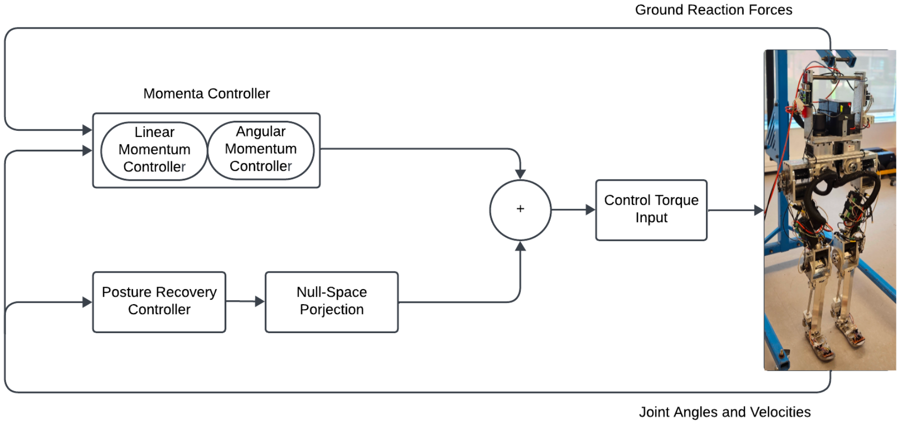

Figure 18: Block diagram of the proposed push recovery control.

4.4 Summary

This section presented our proposed push recovery control, which employs the principles of momentum theory to ensure stability when exposed to external pushing forces. Section 4.2.1 introduced the proposed **Variable Power Rate Reaching Law**, which aims to stabilize the linear momentum of our robot (HURON). In section 4.2.2, we examined two approaches for defining the desired rate of change of angular momentum. The process of establishing a task of **Lower Priority** to restore the robot to an upright position without causing any disruption to the momentum controllers was described in section 4.3.

5 Results and Discussion

This section will show the findings obtained from our proposed push recovery control, which were designed to ensure standing stability. As stated in 4.2.2, the desired $\dot{H}_{CoM,y}$ is defined in two different approaches. Therefore, in this part, we analyze the proposed control for both approaches.

5.1 Performance of Proposed Control using the First Approach of $\dot{H}_{CoM,y}$

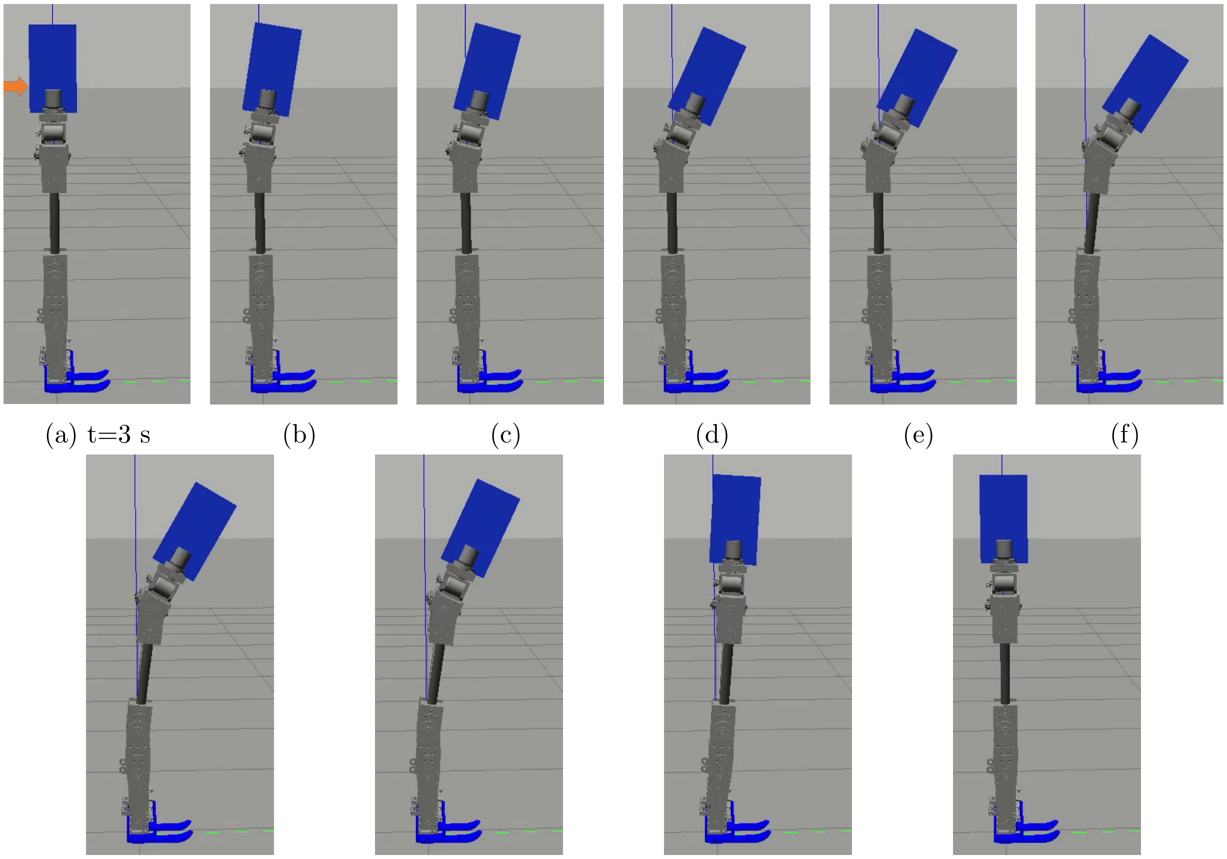

(a) t=3 s (b) (c) (d) (e) (f)

(g) (h) (i) (j) t=5.2 s

Figure 19: The simulation response to 80 N at 0.1 m from the hip joint (waist) for 0.1 sec. with the **First Approach** (https://www.youtube.com/watch?v=zvh4cghN9b8).

Table 3: Control Parameters.

Parameter	Value
λ	1.9
k_1	0.001
k_3	7
σ	1
η	1
k_H	3
K_q	diag [1.95,1.95,1.95]
λ_q	diag [6.1, 6.1, 6.1]
ϵ	1 for all joints

To evaluate the efficacy of the proposed push recovery control, an analysis was conducted on the performance of the control algorithm within a simulated environment (Gazebo). A pushing force of 80 N for a duration of 0.1 sec. is exerted at 0.1 m from the hip joint (waist), as seen in Fig. 19a. Table 3 illustrates the control parameters. The effectiveness in preserving the stability and upright position of the robot is depicted in Fig. 19. The peak of the CoP is measured to be 0.122 m, which is below the maximum limit of 0.18 m, as depicted in Fig. 22. Additionally, it is worth mentioning that the robot demonstrates a recovery period of 2.23 sec. following the application of the pushing force. This characteristic potentially allows the robot to withstand multiple successive pushes within a short time period. The magnitude of the error in the steady state for both the CoP and CoM is 0.0002 m, as depicted in Fig. 22 and Fig. 23

The proposed control also demonstrates apparent effectiveness in mitigating chattering in joint torques, as well as eliminating oscillations, as shown in Fig. 20. The ankle, knee, and hip joints exhibit maximum torques of 19, 18.1, and 10.4 N.m, respectively. The use of the null-space for posture recovery is depicted in Fig. 21, demonstrating the robot's recovery of an upright standing posture with minimal interference to the main controllers, specifically the momenta controllers. Upon analyzing the movement of the joints, it is evident that the knee and hip joints demonstrate forward rotation with angular displacements of -0.11 and -0.57 rad, respectively. In contrast, the ankle joint exhibits an initial backward displacement of 0.03 rad, succeeded by a forward rotation of -0.108 rad. This behavior exhibits similarities to the human response to pushing.

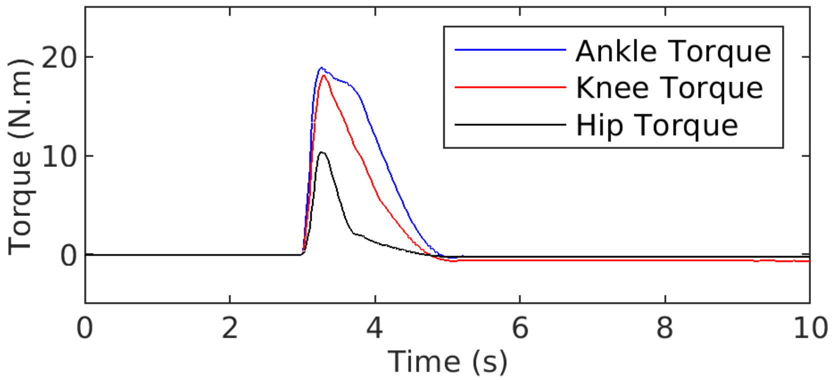

Figure 20: Joint Torques of the proposed control with the **First Approach** at a pushing force 80 N at 0.1 m from the hip joint (waist) for 0.1 sec.

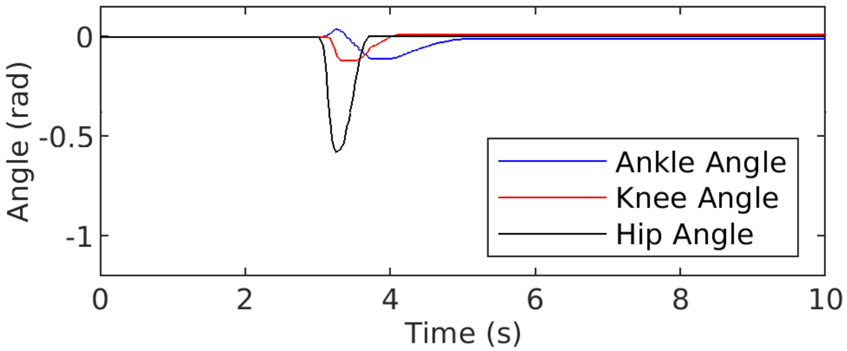

Figure 21: Joint Angles of the proposed control with the **First Approach** at a pushing force 80 N at 0.1 m from the hip joint (waist) for 0.1 sec.

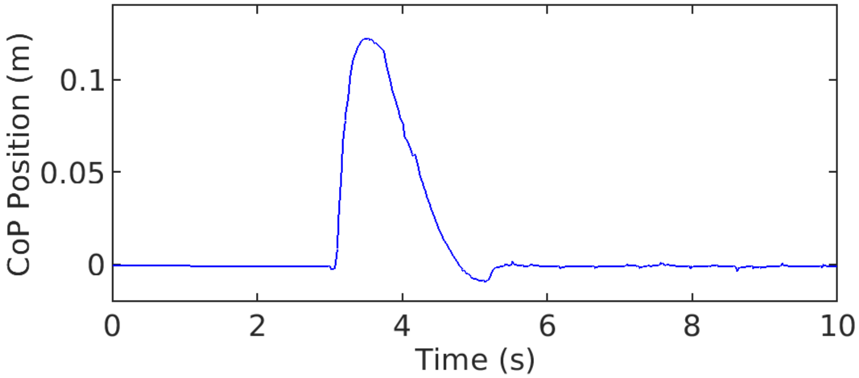

Figure 22: CoP Position of the proposed control with the **First Approach** at a pushing force 80 N at 0.1 m from the hip joint (waist) for 0.1 sec.

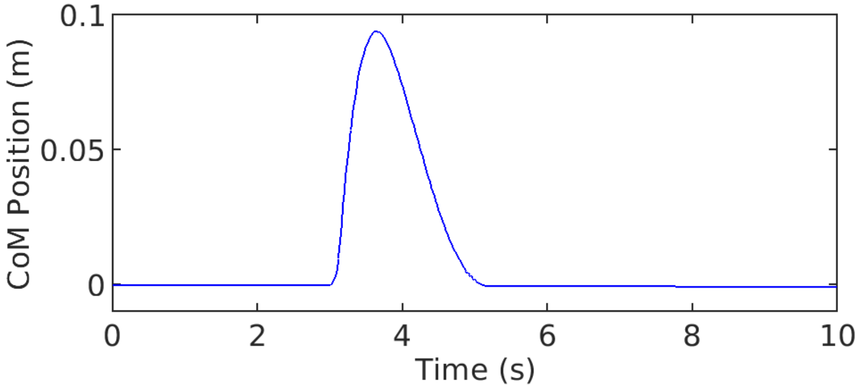

Figure 23: CoM Position of the proposed control with the **First Approach** at a pushing force 80 N at 0.1 m from the hip joint (waist) for 0.1 sec.

5.2 Performance of Proposed Control using the Second Approach of $\dot{H}_{CoM,y}$

To determine the effectiveness of the **Second Approach** utilized in the angular momentum controller, a repetition of the test conducted in the first section of the findings was performed. It is essential to highlight that a second-order Low Pass Filter (LPF) was utilized to reduce the impact of noise in the signals of $F_{GR,z}$. This action was undertaken due to the fact that the desired rate of angular momentum change is dependent upon the force exerted by the ground in the vertical direction $F_{GR,z}$, as well as the position of the CoP. Fig. 24 demonstrates the efficacy of the proposed control method in preserving the balance and upright position of the robot when subjected to external pushing forces. It is noteworthy to remark that this study exclusively considers the positive $\dot{H}_{CoM,y}$ component, which corresponds to the direction of the applied force, in order to counterbalance the external disturbances. Fig. 25a shows the the positive $\dot{H}_{CoM,y}$ generated in the **Second Approach** due to the applied pushing force and the difference between the CoP and CoM positions, as shown in 25b. We can also see that this rate of change diminishes to zero when the CoP aligns with the CoM position. This reasoning is reasonable since the momentum produced around the CoM, denoted as $\dot{H}_{CoM,y}$, arises from the disparity between the positions of the CoP and the CoM, as indicated in equation (11). It is also noticeable that the difference between the CoP and CoM positions can be negative, as shown in Fig. 25b, which requires counterclockwise $\dot{H}_{CoM,y}$. However, the difference value is so small, and consequently the counterclockwise $\dot{H}_{CoM,y}$ can be neglected.

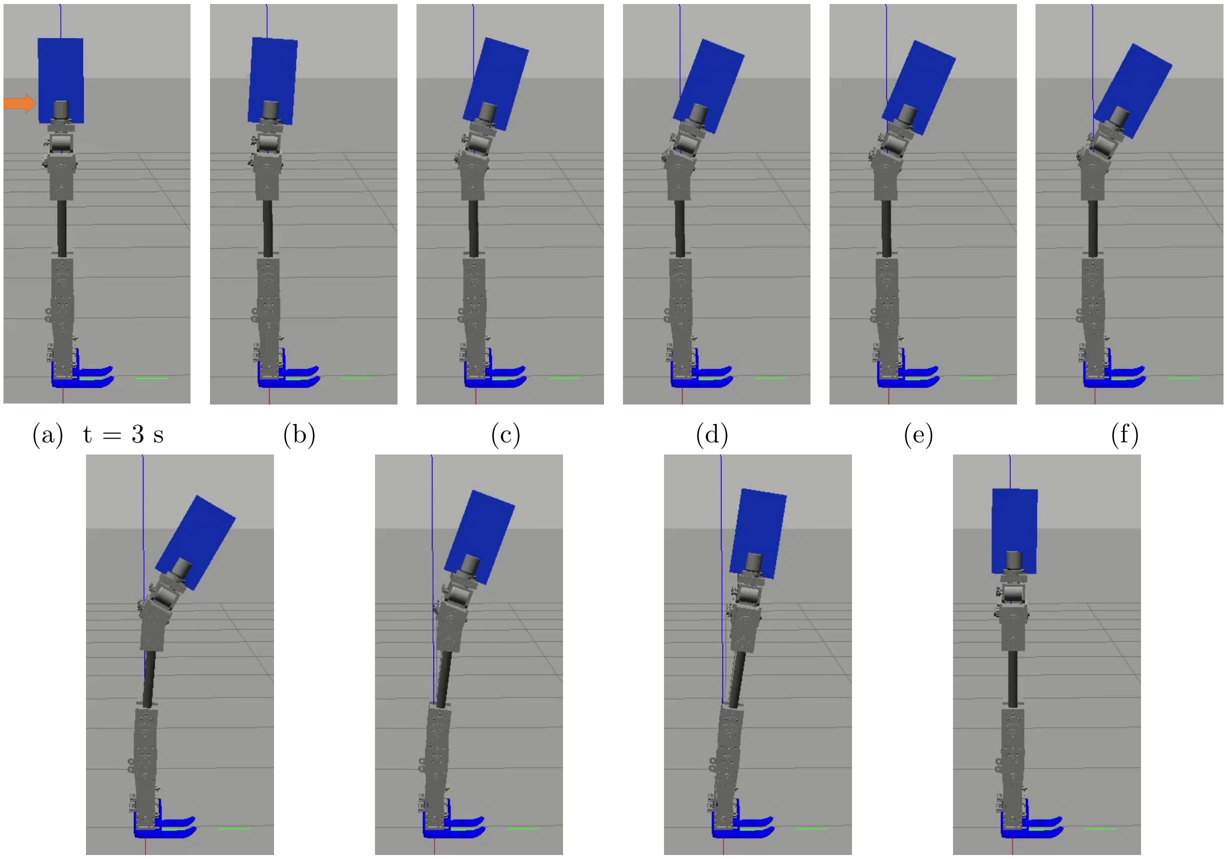

(a) t = 3 s (b) (c) (d) (e) (f)

(g) (h) (i) (j) t = 5.2 s

Figure 24: The simulation response to 80 N at 0.1 m from the hip joint (waist) for 0.1 sec. with the **Second Approach**.

In Fig. 26, the joint torques are depicted, with the ankle, knee, and hip joints demonstrating peak torques of 18.8, 15.8, and 9.9 N.m, respectively. Upon analyzing Fig. 27, it becomes apparent that the knee and hip joints demonstrate a forward rotation. This is supported by the angular displacements of -0.075 and -0.57 rad observed in these joints, respectively. Conversely, the ankle joint exhibits an initial backward displacement of 0.01 rad, succeeded by a forward rotation of -0.09 rad.

Fig. 28 shows that the peak of the CoP is measured at 0.116 m, with a maximum variance of ±0.002 m across all simulation iterations, attributed to the presence of noisy GRF. The steady-state error for both CoP and CoM is 0.001 m, as depicted in Fig. 28 and Fig. 29. As as result, there is an approximate reduction of 6 mm in the peak CoP. This indicates that the **Second Approach** exhibits improved stability when subjected to a higher pushing force.

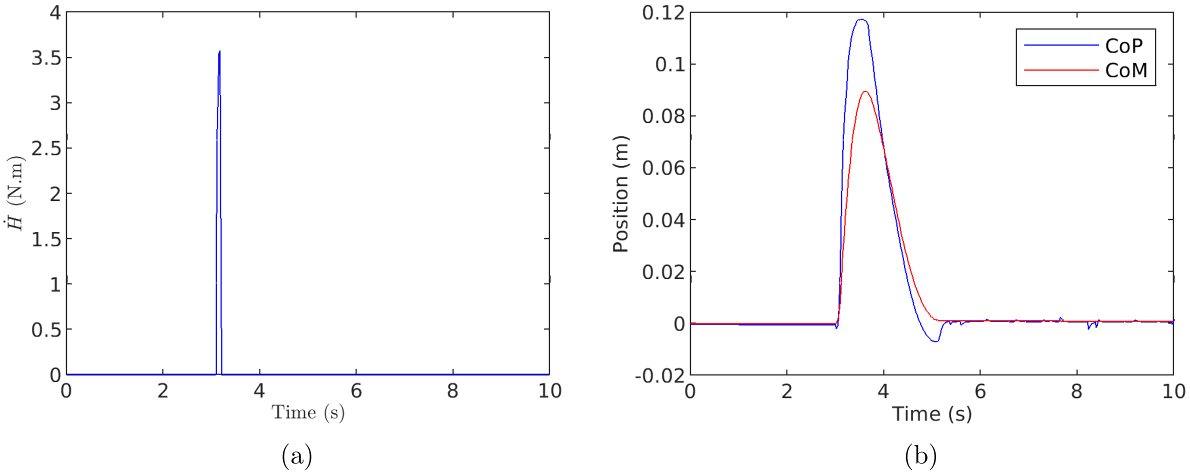

Figure 25: Proposed control with the **Second Approach** (a) Rate of change of angular momentum defined in equation (42) , (b) CoP-CoM position.

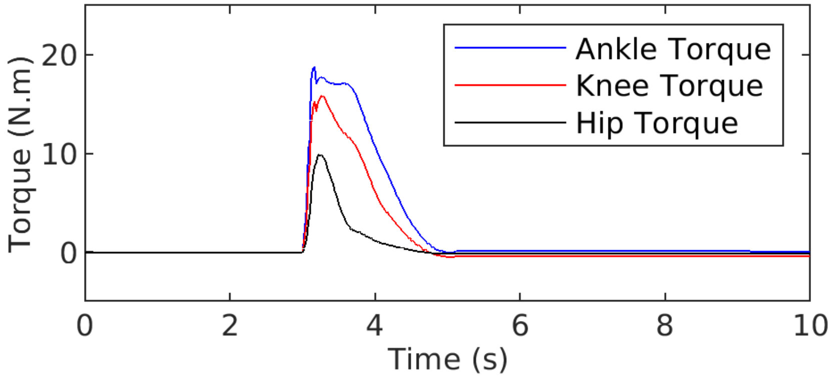

Figure 26: Joint Torques of the proposed control with the **Second Approach** at a pushing force 80 N at 0.1 m from the hip joint (waist) for 0.1 sec.

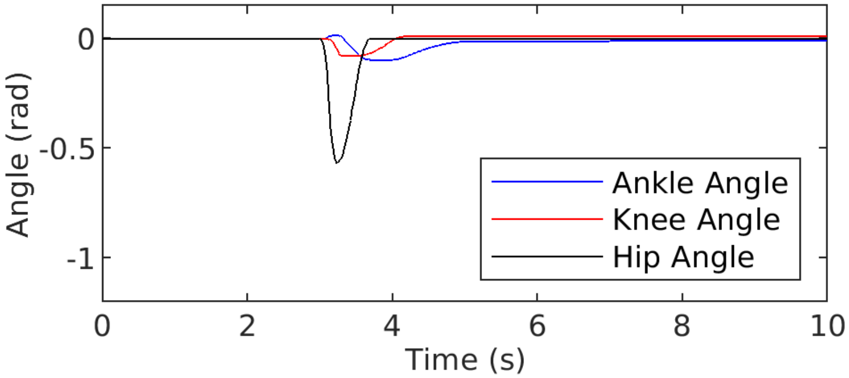

Figure 27: Joint Angles of the proposed control with the **Second Approach** at a pushing force 80 N at 0.1 m from the hip joint (waist) for 0.1 sec.

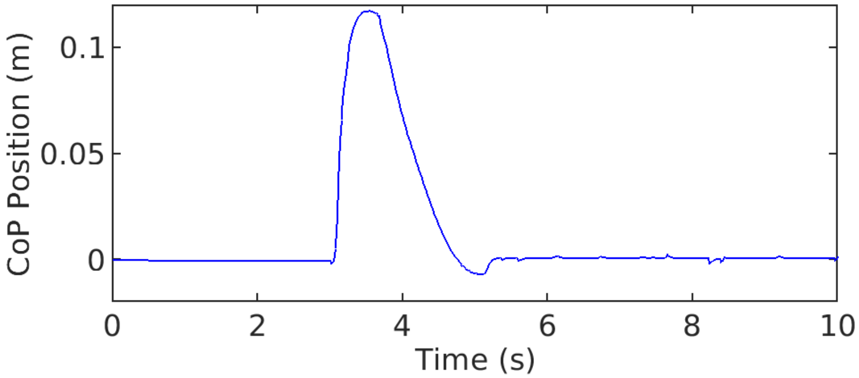

Figure 28: CoP Position of the proposed control with the **Second Approach** at a pushing force 80 N at 0.1 m from the hip joint (waist) for 0.1 sec.

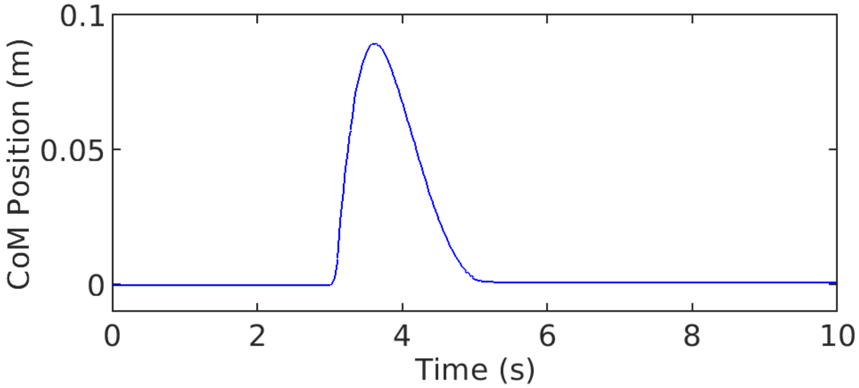

Figure 29: CoM Position of the proposed control with the **Second Approach** at a pushing force 80 N at 0.1 m from the hip joint (waist) for 0.1 sec.

To examine the performance of the proposed control using the **Second Approach** of $\dot{H}_{CoM,y}$ with **varying external disturbance locations**, an external force of 80 N is applied at a distance of 0.2 m from the hip joint (waist) for a duration of 0.1 sec. as shown in Fig. 30a. The efficacy of the proposed push recovery control utilizing the **Second Approach** of angular momentum is evident in its ability to maintain stability and an upright posture when faced with external forces located at higher positions from the waist, as depicted in Fig. 30. The joint torques and angles are illustrated in Fig. 31a and Fig. 31b, respectively. It is also clear in Fig. 32a and Fig. 32b that the maximum positions of the CoP and CoM as 0.114 and 0.09 m, respectively.

Previous research, as the one conducted in [6], employed a push recovery control system that switches between **Disturbance Avoidance Phase** and the **Posture Recovery Phase**. If the robot is pushed during the **Posture Recovery Phase**, the control system does not initiate the

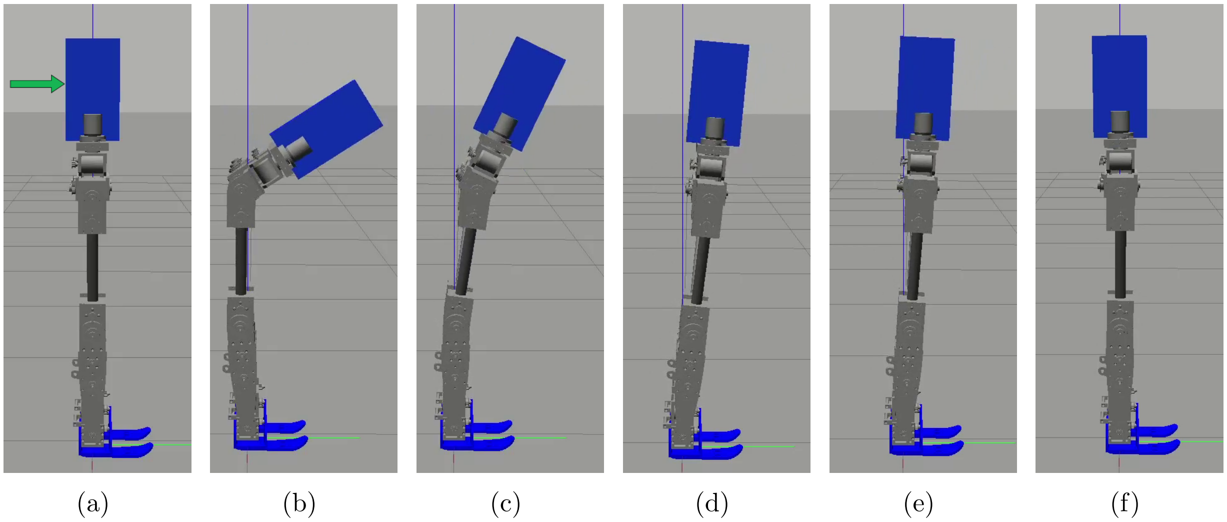
(a) (b) (c) (d) (e) (f)

Figure 30: The simulation response to 80 N at 0.2 m from the waist (**higher disturbance location**) for 0.1 sec. with the **Second Approach** (https://www.youtube.com/watch?v=IDqmpjjPu2g).

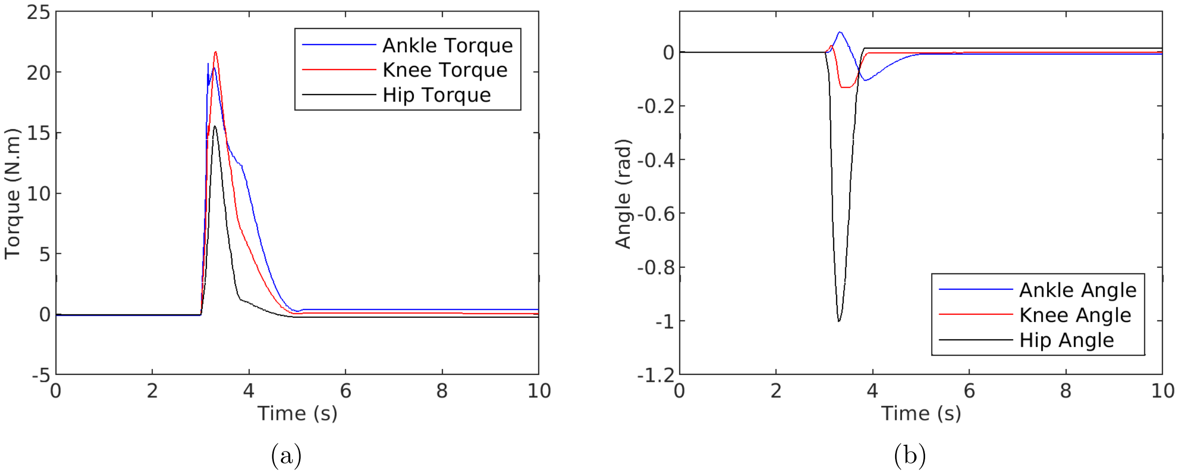

(a) (b)

Figure 31: Proposed control performance to 80 N at 0.2 m from the waist (**higher disturbance location**) for 0.1 sec. with the **Second Approach** (a) Joint Torques, (b) Joint Angles.

Disturbance Avoidance Phase to stabilize the linear and angular momenta. Disabling the momentum controllers causes the system to function as a stiff pendulum model, with just the joint space control in the **Posture Recovery Phase** being active. By exclusively relying on the joint space control, the CoP is pushed towards the front of the foot, ultimately resulting in a loss of balance and subsequent fall. As we mentioned earlier, in this study we propose using the null-space method to simultaneously execute both the **Disturbance Avoidance Phase** and the **Posture Recovery Phase**. We conducted another experiment by **exerting force on the robot on two**

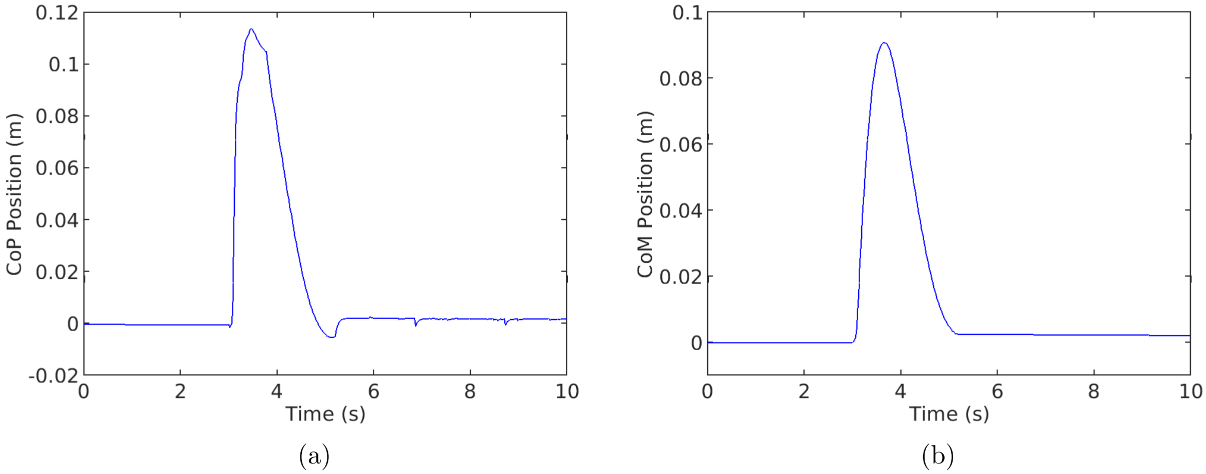

(a) (b)

Figure 32: Proposed control performance to 80 N at 0.2 m from the waist (**higher disturbance location**) for 0.1 sec. with the **Second Approach** (a) CoP Position, (b) CoM Position.

separate times. The initial push of 60 N is applied with a distance of 0.1 m from the (waist) and a duration of 0.1 sec. as shown in Fig. 33a. The second push occurs after one second from the first push, as shown in Fig. 33c, when the robot is returning to an upright position. Fig. 33 illustrates the ability of our robot (HURON) to maintain balance and an upright posture, even when subjected to two successive pushing forces. It is worth noting that there is an error of around 0.013 rad in the ankle and hip angle joints, and 0.019 rad in the knee joint as shown in Fig. 34b. Tuning the parameters in Table 3 may potentially decrease the errors in the joint angles.

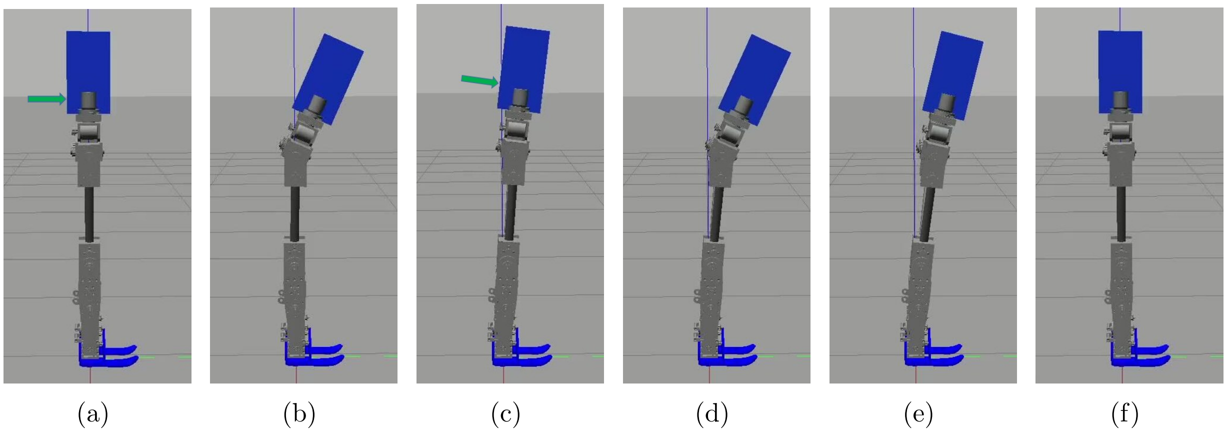

(a) (b) (c) (d) (e) (f)

Figure 33: The simulation response to 60 N at 0.1 m from the waist for 0.1 sec. with the **Second Approach** with **two successive pushing forces** separated by one second. More tests can be found https://www.youtube.com/watch?v=aWAKxNK5P1Y

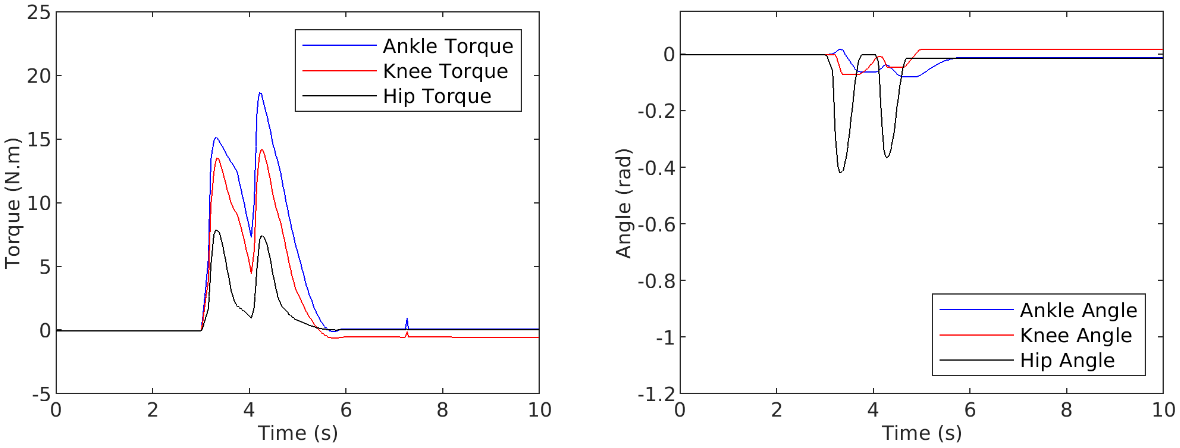

(a) (b)

Figure 34: Proposed control performance to 60 N at 0.1 m from the waist for 0.1 sec. with the **Second Approach** with **two successive pushing forces** separated by one second. (a) Joint Torques, (b) Joint Angles.

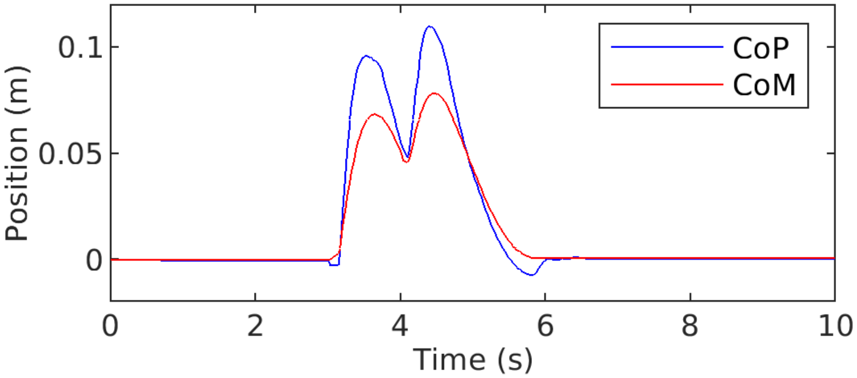

Figure 35: CoP and CoM positions of the proposed controller with the **Second Approach** at a pushing force 60 N at 0.1 m from the waist for 0.1 sec. with **two successive pushing forces** separated by one second.

5.3 Comparison with other Controllers

To compare our proposed push recovery control to previous works, the following four controllers were chosen:

1) Benjamin's controller [5]: A balance controller that enables a humanoid to maintain a standing position while recovering from disturbances. This controller consists of two sub-controllers as shown in Fig. 36. The first one is the unconstrained balance controller, which calculates the appropriate torques without imposing any constraints on the position of the CoP. The unconstrained

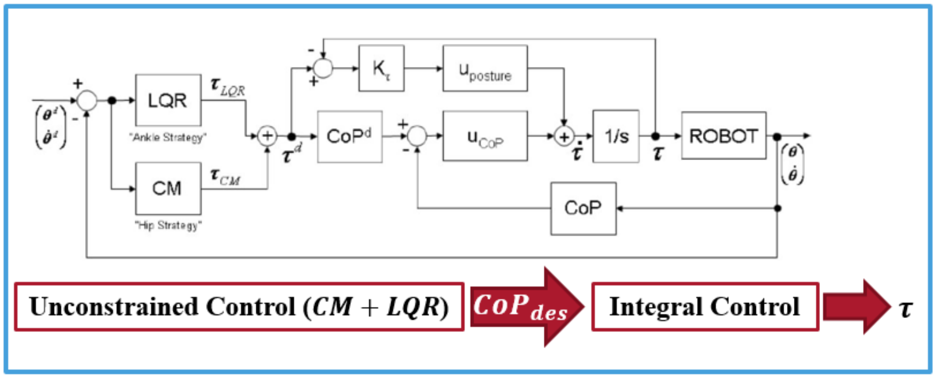

Figure 36: Benjamin's controller [5].

balance controller employed joint space LQR (to drive the joint angles to zero) and CoM controller (to drive the CoM to zero). However, the torque produced by these unrestricted controllers was just utilized to determine the desired position of the CoP. Afterward, the second controller, a decoupled integral controller, was employed to control the position of the CoP precisely. Posture recovery is not used here since CoP does not depend on the torque from posture recovery.

Benjamin's controller was chosen to compare our *Momentum-Based Control Strategy* with the CoP integral controller presented in [5].

The parameters used in simulation are: $k_{CMp} = 20$, $k_{CMd} = 5$, $k_{CoP} = 10$,

$$k_{LQR} = \begin{bmatrix} 274.7973 & 32.8129 & 82.9994 & 10.9307 \\ 21.6590 & 30.5036 & 7.7975 & 2.7605 \end{bmatrix}$$

2) Abdallah *et al.* [6]: A control technique consists of two phases aiming to maintain balance in a force disturbance as shown in Fig. 37. During the reflex phase, the desired momentum change rate was determined to be $\dot{L}_x = -k_2 L_x$ and $\dot{H}_{CoM} = -k_1(CoP_x - CoM_x)$. This phase was responsible for mitigating the destabilizing effects of the disruption. The second phase, known as the recovery phase, was responsible for moving the robot to a stable static posture. The authors of [6] stated that maximizing the potential energy or minimizing the static joint torques $G(q)$ leads to achieving a static stable configuration. We have built the Hessian method, which minimizes the function $G(q)$. The control law for determining the minimal G was established by developing a relationship between the rate of change of G and the joint velocities $\dot{q}$, ($\dot{G} = J(q)\dot{q}$). The desired

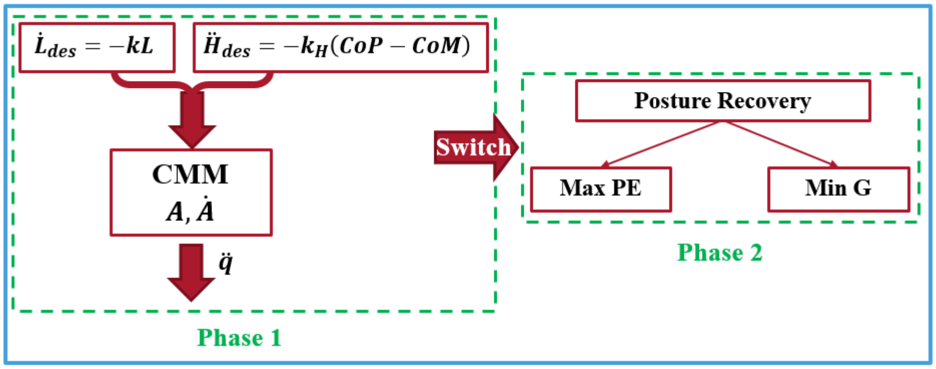

Figure 37: Abdallah *et al.* controller [6].

acceleration was $\ddot{q} = -k(\dot{q} + \dot{J}^{-1}G)$. The parameters used in simulation are: $k_1 = 1$, $k_2 = 2$, $k = 1.5$.

3) Constant Power Rate Reaching Law (CPRL)/Constant Rate Reaching Law (CRRL): In the linear momentum controller, we initially replaced the proposed **Variable Power Rate Reaching Law** with CPRL (Constant Power Rate Reaching Law) and subsequently substituted it with CRRL (Constant Rate Reaching Law). The controllers were chosen to showcase the chattering issue, the error steady state difficulty, and the efficacy of the proposed SMC in addressing these problems. For the angular momentum controller, we employed the **First Approach**. We utilized the same posture recovery approach presented in this study.

Linear sliding surface: $s = \dot{e} + \lambda e$

Constant Power Rate Reaching Law: $\dot{s} = -k|s|^{\rho} sat(s/\phi)$

The parameters used are: $\lambda = 2.2$, $k = 1$, $\rho = 3$ and $\phi = 0.6$.

Constant Rate Reaching Law: $\dot{s} = -k\ sgn(s)$

The parameters used are: $\lambda = 2.2$, and $k = 0.05$.

4) Linear Quadratic Regulator (LQR): The control law is defined as $\tau_{LQR} = -k_{LQR} \begin{bmatrix} q \\ \dot{q} \end{bmatrix}$

$$k_{LQR} = \begin{bmatrix} 228.34 & 111.03 & 22.24 & 68.03 & 39.21 & 8.41 \\ 203.29 & 177.38 & 40.38 & 64.42 & 42.24 & 10.12 \\ 6.83 & 8.60 & 26.82 & 2.76 & 2.69 & 1.79 \end{bmatrix}$$

Table 4: Controllers used for comparison.

Controller	Comparison criteria
1) Benjamin's controller [5]	1) To compare our *Momentum-Based Balance Strategy* with CoP integral controller presented in [5].
2) Abdallah *et al.* controller [6]	2) To show the superiority of our proposed push recovery control over the simple controllers presented in [6].
3) CPRL/CRRL SMC	3) To show the chattering issue, the error steady state difficulty, and the efficacy of the proposed SMC in addressing these problems.
4) Joint space LQR	4) To show a joint space control in which the CoP has no control, showing the importance of CoP control presented by our approach.

The LQR was chosen for comparison because it is a joint space control in which the CoP has no control, showing the importance of CoP control presented by our approach. Table 4 lists the controllers that were used for comparison and explains why those controllers were chosen.

In this study, the control settings of the aforementioned controllers were fine-tuned to ensure their best performance on our bipedal robot (HURON) in terms of achieving the minimum CoP distance from the reference frame. We implemented all the controllers within a wide range of forces from low to high forces.

5.3.1 CoP Comparison under Low Pushing Force

Fig. 38 displays the CoP comparison under a 45 N force applied for 0.1 sec. at 0.1 m from the waist. LQR and Benjamin's controller [5] show higher CoP peaks at 0.132 and 0.179 m, respectively. The joint space LQR is anticipated to result in a high CoP position, as its purpose is to drive the joint angles to zero without imposing any restrictions on the CoP position. The robot equipped with the joint space LQR controller exhibits characteristics similar to a stiff inverted pendulum, without the ability to avoid disturbances by generating angular momentum to accelerate forward. The knee joint in Benjamin's work [5] was considered locked, simplifying the robot model through a two-link robot model. This simplification could potentially result in the loss of the ability of the knee joint to absorb disturbances. These, together with ignoring dynamics uncertainties in an ideal simulation environment, might be the possible reasons why Benjamin's controller is not showing satisfactory results in Fig. 38.

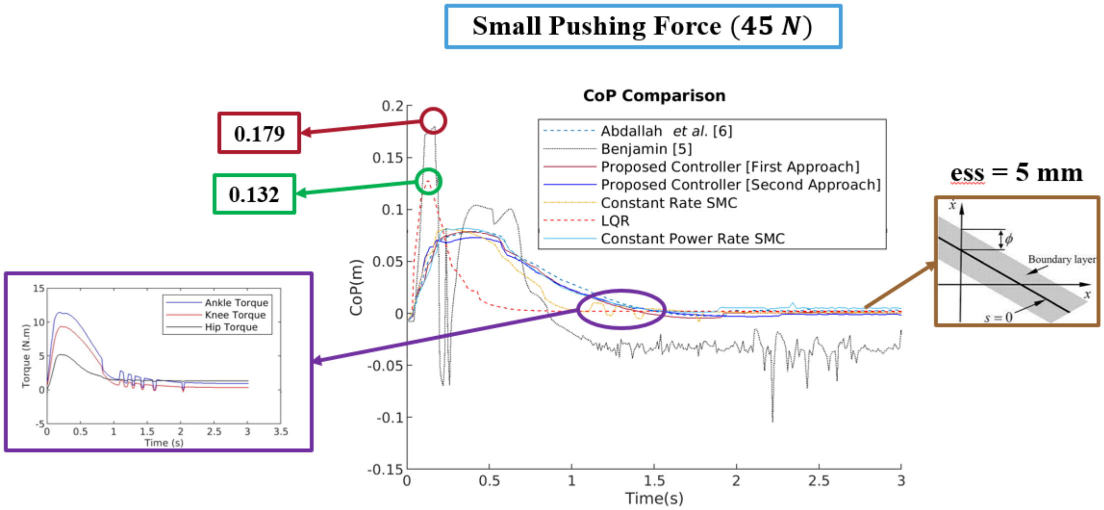

Figure 38: CoP position comparison is simulated for 3 sec. with disturbance 45 N for 0.1 sec.

Upon performing an analysis of the Constant Rate SMC, it becomes apparent that the joint torques exhibit chattering, as illustrated in Fig. 39. Chattering is the consequence of the irregular movement of the Center of Pressure (CoP) caused by the torques applied to the joints. To address the issue of chattering, we utilized a saturation function in combination with the Constant Power Reaching Law. However, this solution led to a steady-state error of 0.005 m in the CoP position. It is obvious that the proposed **Variable Power Reaching Law** eliminates the chattering issue while providing a small steady-state error of 0.0004 m in the CoP position .

The CoP peaks for the proposed controller (**First Approach**), proposed controller (**Second Approach**), Constant Power Rate SMC, Constant Rate SMC and Abdallah *et al.* [6] are 0.078, 0.073, 0.082, 0.080 and 0.078 m, respectively. Although the proposed controller has the lowest CoP value, the reduction compared to Constant Power Rate SMC, Constant Rate SMC and Abdallah *et al.* [6] is not statistically significant. This is partly due to the similarity in behavior among all three momentum-based controllers when low forces are applied. Another experiment with a high force of 75N was conducted to distinguish controller behaviors, as described in the next section.

5.3.2 CoP Comparison under High Pushing Force

Fig. 40 shows the CoP comparison under a 75N force applied for 0.1 sec. LQR and Benjamin's controllers [5] proved to be ineffective under high-force conditions. The comparison with high

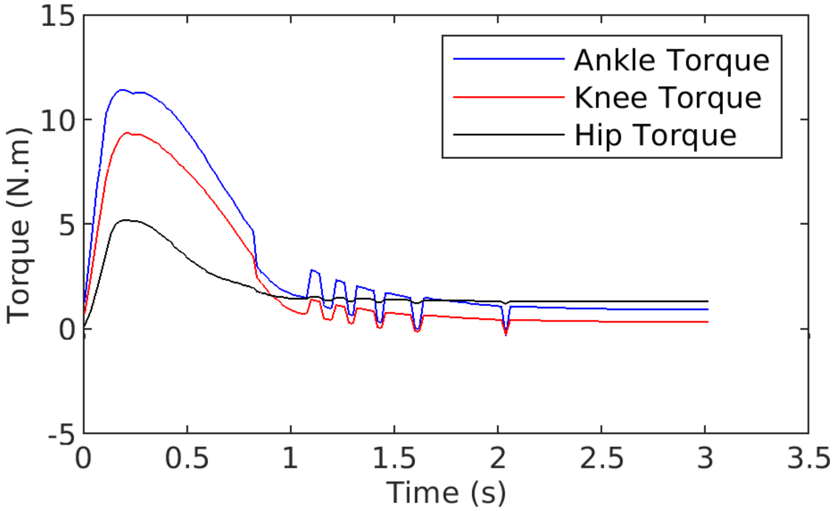

Figure 39: Joint torques of the Constant Rate Reaching Law for linear momentum, **First Approach** of angular momentum controller, and the same posture recovery controller.

pushing force does not include the Constant Rate and Constant Power SMC controllers because they were only used to emphasize the chattering and steady-state error problems.

The proposed controller (**First Approach**), proposed controller (**Second Approach**), and Abdallah *et al.* [6] have CoP peaks of 0.120, 0.116, and 0.167 m, respectively. Given that the proposed push recovery control using the **Second Approach** yields the smallest CoP position, we can infer that our robot (HURON) can maintain standing stability even when subjected to large pushing forces. The high CoP position observed in [6] is likely due to the implementation of a simple proportional controller for linear momentum.

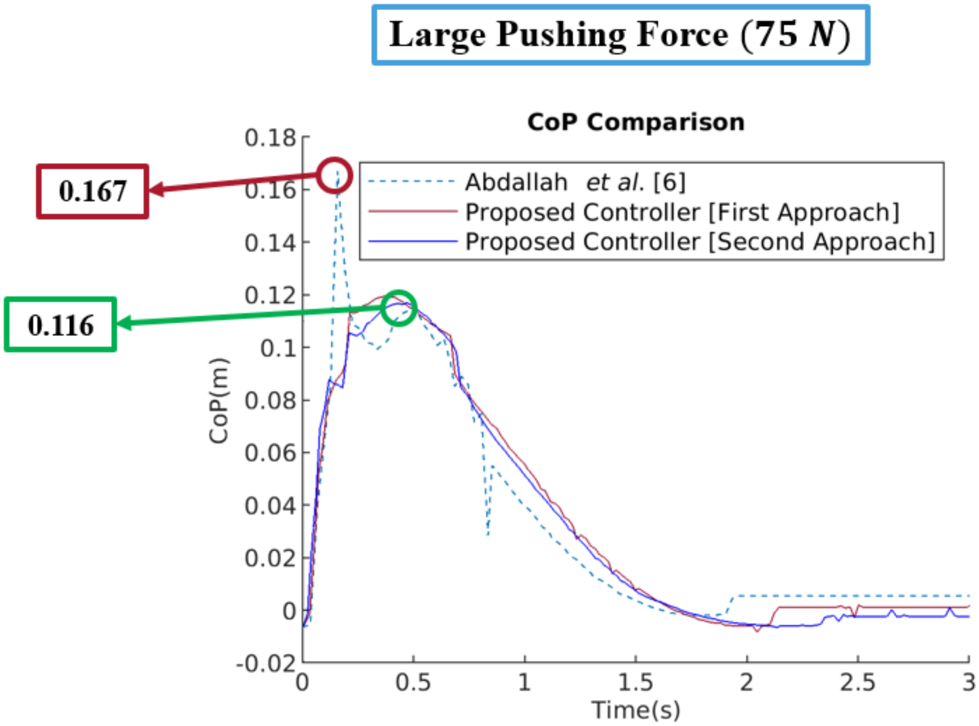

Figure 40: CoP position comparison is simulated for 3 sec. with disturbance 75 N for 0.1 sec.

5.3.3 Maximum Force Tolerance

We continued our comparison scenarios by increasing the pushing force to find the maximum force tolerated by each controller before the bipedal robot (HURON) loses stability. The results showed that our proposed control (**Second Approach**) is able to withstand a force of 117 N applied for 0.1 sec. making it the most robust among the other controllers as described in Fig. 41. This maximum force was 52% higher than Abdallah *et al.* [6], 113% higher than LQR's, and 134% higher than Benjamin's controller [5].

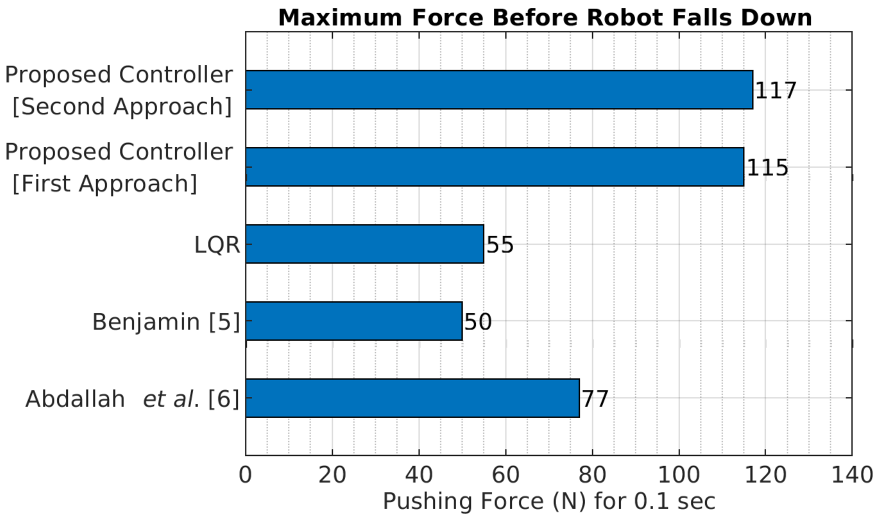

Figure 41: Maximum force before robot falls down.

5.4 Summary

The results of implementing the proposed push recovery control utilizing both approaches of the angular momentum controller were analyzed and discussed. Then, experiments were conducted to prove that the proposed push recovery method works even when there are several pushing forces in a sequence. Lastly, this section showed how our proposed control system is superior to others in maintaining upright stability in the face of substantial external disruptions.

6 Conclusion

In this thesis, we have presented a momentum-based push recovery control method for bipedal robots. We have proposed a **Variable Power Rate Reaching Law-Based SMC** to stabilize the linear momentum of bipedal robots. The proposed reaching law can not only eliminate chattering, but also achieve quick convergence and make the system approach the sliding mode surface in finite time from any point, regardless of its distance from or closeness to the surface. The desired rate of change of angular momentum about the CoM was defined using two approaches. In the **First Approach**, the desired rate of change of angular momentum was defined as the difference between the positions of the CoP and CoM. While in the **Second Approach**, the desired rate of change of angular momentum around the CoM was determined by considering the desired rate of change of linear momentum, the difference between the positions of the CoP and CoM, and the normal component of the ($F_{GR,z}$). We also proposed using the null-space method to restore the robot to the upright posture without interfering with its main momentum controllers. The Higher Priority task is for the momenta controllers (**Disturbance Avoidance Phase**), while the Lower Priority task is for **Posture Recovery Phase**.

The results demonstrated the effectiveness of our proposed push recovery control in maintaining the standing stability of our bipedal robot (HURON) under high external forces while addressing the chattering problem. Additionally, the results demonstrated the ability of our robot to maintain balance and an upright posture, even when subjected to two successive pushing forces separated by one second, which can be attributed to perform both phases simultaneously by using null-space method. Comparing with other established controllers, our proposed controller showed superior performance in keeping the CoP within the support polygon with minimum CoP peak, resulting in tolerating higher pushing forces (up to 117 N for 0.1 sec.).

7 Ongoing Study and Future Works

This section introduces our ongoing study, focusing on the implementation methodology of the push recovery control by stepping. Furthermore, this section presents our future works.

7.1 Stepping-Based Push Recovery Control: Ongoing Study

We introduce our approach that allows our robot (HURON) to execute a step in the presence of substantial pushing forces that exceed the limits of standing stability.

7.1.1 Background of Stepping-Based Stability

It is generally understood that bipedal robots, such as humanoids, need to take steps to prevent falling when they experience a force of significant magnitude that cannot be mitigated by standing balance control. **When and where** to take a step has been an ongoing topic. A systematic method for calculating the Capture Point (CP) and the Capture Region is described in [48] [7]. A Capture Point is a location on the ground where the robot can step to come to a complete stop. A Capture Region is made up of all Capture Points. Simplified models are used to find the Capture Point because the physics of walking on two legs is complex, non-linear, and hybrid. For the Linear Inverted Pendulum Model (*LIPM*), Orbital Energy [3], a conserved component, is employed to compute the Capture Point. Fig. 42 shows a schematic representation of 3D-*LIPM* with a point foot.

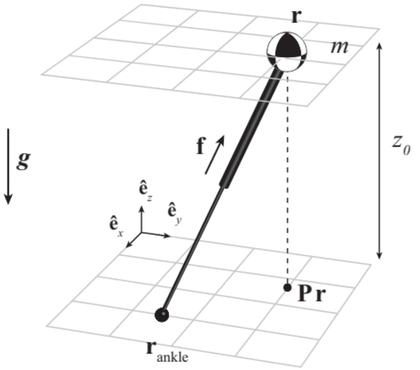

Figure 42: 3D-LIPM with point foot [7].

where $g = [0, 0, -g]^T$, $f = [f_x, f_y, f_z]^T$, $r = [x_{CoM}, y_{CoM}, z_0]^T$, P projects r onto the xy-plane, and $r_{ankle} = [x_{ankle}, y_{ankle}, z_{ankle}]^T$.

The equation of motion in x direction is

$$\ddot{x}_{CoM} = \frac{g}{z_0}(x_{CoM} - x_{ankle}) \tag{59}$$

The Orbital Energy is defined as

$$E_{LIP,x} = \frac{1}{2}(\dot{x}_{CoM})^2 - \frac{g}{2z_0}(x_{CoM} - x_{ankle})^2 \tag{60}$$

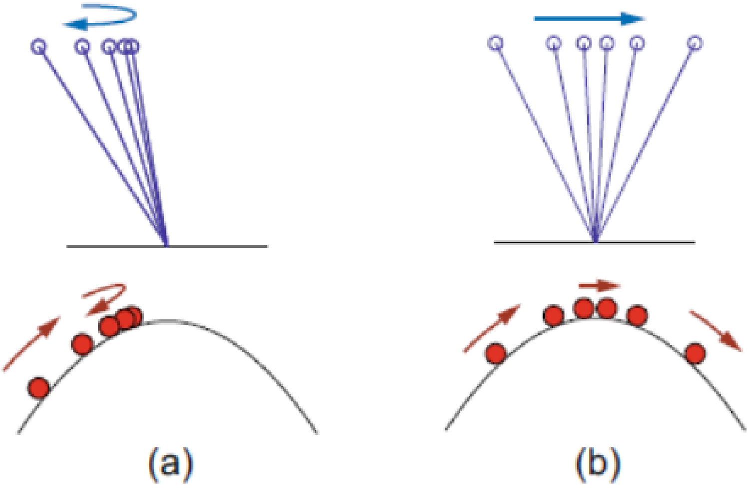

Figure 43: Orbital Energy of *LIPM.* (a) The CoM's initial velocity is insufficient to allow it to pass over the ankle joint point, (b) the case when the initial velocity of the CoM is sufficient [3].

Fig. 43 illustrates how the Orbital Energy determines the behavior of the pendulum. If $E_{LIP,x} < 0$, there is insufficient energy for the x_{CoM} to reach x_{ankle}. If $E_{LIP,x}$ is more than zero, there is sufficient energy for the center of mass x_{CoM} to reach x_{ankle} and accelerate away from it. If $E_{LIP,x}$ is equal to zero, it indicates that the horizontal position of the center of mass, x_{CoM}, comes to a complete stop precisely at the position of the ankle, x_{ankle}.

Therefore, the foot placement required to obtain zero Orbital Energy is essential. Solving equation (60) for x_{ankle} when $E_{LIP,x} = 0$ to compute the Instantaneous Capture Point (ICP).

$$x_{capture} = x_{CoM} + \frac{\dot{x}_{CoM}}{\sqrt{\frac{g}{z_0}}} \tag{61}$$

Equation (61) demonstrates that the Capture Point is dependent on the CoM's position and velocity, suggesting that only linear momentum is considered. The authors of [7] expanded the Linear Inverted Pendulum to the Linear Inverted Pendulum Plus Flywheel Model to account for the effect of angular momentum on the calculation of Capture Point, which will grow to a Capture Region. More details can be found in [48] [7]. [49] and [50] introduced a control system for bipedal walking based on the Capture Point dynamics. The Capture Point control, as described in [49], was developed using the natural dynamics of the *LIPM*. The research in [50] further expanded on the concepts proposed in [49] by utilizing a Model Predictive Control (MPC) framework. Instead of using a 3D Linear Inverted Pendulum with a point foot, the authors of [51] chose to use a LIPM with a finite-size foot model. The current Capture Point, foot edge, and foot position were used to determine a "do not step" condition.

Researchers have proposed utilizing human motion data to construct stepping balance control for human-like robots, as human balance methods, such as stepping stability, are considered reliable methods for creating robust and efficient systems. The authors [52] introduced a technique for generating a motion that counteracts disturbances and preserves balance. This method relies on a simplified mechanism and is inspired by observations of human movement. The initial phase in [52] was analyzing human motion to identify fundamental characteristics. Subsequently, a simple structure, such as an inverted pendulum model, was employed to choose the desired foot placement, with its parameters derived from human motion. Meanwhile, [53] selected the required step position so that the center of mass will be positioned precisely at the center of the support polygon after taking the step.

Our study does not use the energy-based method that uses the Capture Point concept to determine **when and where** to step, nor the human motion data. Our study focuses on using *Momentum-Based Control* to recover balance in bipedal robots. We determine **when and where** to respond to external forces by evaluating momenta as described in [8].

7.1.2 Stepping-Based Stability Control: Methodology and Implementation

In section 7.1.2.1, we will illustrate the procedure of determining the position of the step by examining both linear and angular momentum. In the following section, we will describe the methodology through which we generate the desired rate of change of linear and angular momentum, as well as the desired trajectory of the swinging leg. Section 7.1.2.3 will discuss the optimization framework, which includes the objective function and the constraints.

7.1.2.1 Stepping Position based on Momenta

The robot's momenta determine the time and placement of the step for reactive stepping. Unlike the Capture Point concept, which aims to achieve zero Orbital Energy through foot placement, our study uses a momentum-based approach presented in [8] to determine the optimal step location and timing. [8] suggests that a reactionary step might prevent movement by ensuring correct foot positioning. Refer to equation (15), while the third term is neglected, the CoP equation is

$$p_x = c_x + \frac{\dot{H}_{CoM,y} - c_z \dot{L}_x}{\dot{L}_z + mg} \tag{62}$$

Assuming $\dot{L}_x = -d_l.L_x$ and $\dot{H}_{CoM,y} = -d_h.H_{CoM,y}$

where d_l and d_h are damping variables. The new desired CoP which accounts for the desired momentum changes:

$$p_{x,desired} = c_x + \frac{-d_h.H_{CoM,y} + c_z d_l.L_x}{\dot{L}_z + mg} \tag{63}$$

In y direction, the same concept is used as follows:

$$p_{y,desired} = c_y + \frac{-d_h.H_{CoM,x} + c_z d_l.L_y}{\dot{L}_z + mg} \tag{64}$$

The damping variables in the equations stated above dictate the tendency of the robot to take a step. By increasing the values of d_l and d_h, the system's tendency to adopt proactive steps is increased. Low values of the damping variables are used when determining the timing of a step (**when**). On the contrary, in order to determine the precise location of the step (**where**), larger values are selected for the damping variables, as elaborated in [8].

7.1.2.2 Generation of CoM and Swing Leg Trajectories

Biomechanical research have shown that the **trajectory of the CoM** in motion capture data can be accurately represented by a quadratic curve [8]. The reference CoM position (c_r) is generated using a quadratic Bezier curve with three control points. The three points are the CoM's current location, the contact point of the support foot (pivot), and the midpoint between the desired foot placement ($p_{x,desired}$, $p_{y,desired}$) and the support foot (pivot) as shown in Fig. 44. Robot stability can be affected by sudden changes in motion, making it crucial to employ gradual acceleration and deceleration. To achieve this goal, we employ ease-in and ease-out functions to regulate the rate at which an object accelerates or decelerates over a specific period. Consequently, the motion of the CoM initiates with a gradual speed, progressively increases, and then gradually decreases towards the end.

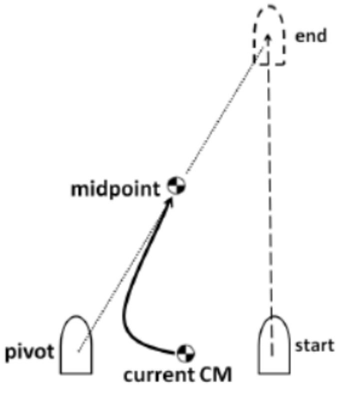

Figure 44: CoM trajectory with quadratic Bezier curve [8].

For swing leg trajectory, we assume that $p_{y,desired} = 0$, indicating that the pushing force is directed towards the center of our robot's back. In this simple case study, the trajectory of the swinging leg is formed in the xz plane. The foot's end position in the x direction is denoted as $p_{x,desired}$. [54] stated that a synthetic Gaussian function is utilized as the speed profile in the x direction. The position trajectory is computed by integrating the Gaussian velocity function, with the final value being $p_{x,desired}$. The acceleration is then computed by taking the time derivative.

For z direction, we choose a Gaussian position function with a height of 10 cm. Fig. 45 depicts the curves for position, velocity, and acceleration in both the x and z directions. The swing leg trajectory does not replicate the normal gait of human beings, but it serves as a more straightforward initial approach. At runtime, using Inverse Kinematics (IK), the reference joint angle (θ_r) is calculated, where the CoM represents the reference frame. The reference joint velocity ($\dot{\theta}_r$) and the reference joint acceleration ($\ddot{\theta}_r$) are estimated through the utilization of finite difference.

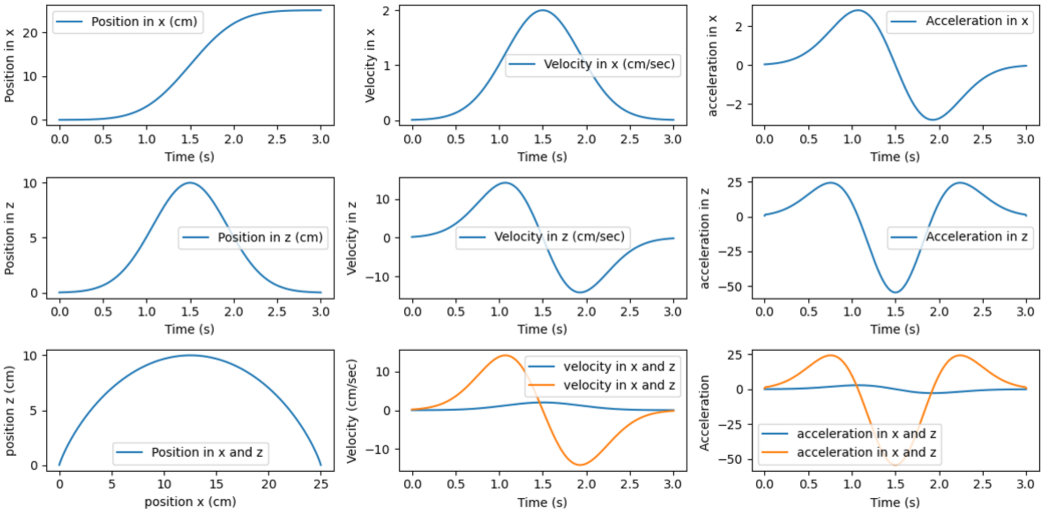

Figure 45: Swing leg trajectory (in this figure, we assume that the $p_{x,desired} = 25cm$ which is equal to the end x position, while the height of the leg is 10 cm).

7.1.2.3 Optimization Framework

The objective function formulation is based on the structure described in [25] [27]. The optimization problem aims to calculate the generalized accelerations ($\ddot{q}$), joint torques (τ), and ground reaction forces (F_{GRF}) by using an objective function. This objective function includes terms that stabilize the rate of change of momenta, as well as a term that tracks the swing leg trajectory during the step. Furthermore, the optimization problem has three constraints: the contact constraint, the dynamic constraint, and the friction cone constraint. These constraints are necessary to maintain stability and satisfy the robot's dynamics.

$$
\begin{aligned}
\underset{\ddot{q},\tau,F_{GRF}}{\text{Minimize:}} \quad & w_1\|\dot{L}_{des} - \dot{L}_{actual}\|^2 + w_2\|\dot{H}_{des} - \dot{H}_{actual}\|^2 + w_3\|\ddot{\theta}_{des} - \ddot{\theta}_{actual}\|^2 \\
\text{Subject to:} \quad & J_c\ddot{q} + \dot{J}_c\dot{q} = 0 \textbf{ (contact constraint)} \\
& M(q)\ddot{q} + C(q,\dot{q})\dot{q} + G(q) = S^T\tau + \sum J_c^T F_{GRF} \textbf{ (dynamic constraint)} \\
& |F_{GRF,t}| \leq \mu F_{GRF,n} \textbf{ (friction cone constraint)}
\end{aligned}
\tag{65}
$$

Weighting factors denoted by w_1, w_2, and w_3 are incorporated into the objective function of a quadratic cost. These weights define the comparative significance of cost function terms. J_c relates $\dot{q} \in \mathbb{R}^{18}$ (floating base and joint velocities) to the velocity of the contact point on the foot. $F_{GRF,t}$ is the tangential ground force, μ is the friction coefficient and $F_{GRF,n}$ is the normal ground force.

The **objective function** as mentioned above consists of three terms: The first term of the objective function is the **Linear Momentum Balance Term**, and as mentioned earlier in section 4.1 controlling the linear momentum is equivalent to controlling the Center of Mass. The desired CoM acceleration is computed using the following equation:

$$\ddot{c}_{des} = k_L(c_r - c) + d_L(\dot{c}_r - \dot{c}) + \ddot{c}_r \tag{66}$$

where $c_r, \dot{c}_r, \ddot{c}_r$ are the reference CoM position, velocity and acceleration respectively, as described in 7.1.2.2. k_L and d_L are tuning parameters. The desired linear momentum rate of change is

$$\dot{L}_{des} = m\ddot{c}_{des} \tag{67}$$

We used centroidal dynamics, a powerful framework provided by Pinocchio, to compute the linear momentum and its derivative of the bipedal robot during dynamics motions. The centroidal dynamics computations are based on the articulated body inertia, joint positions, velocities, and external forces applied to the robot.

The actual linear momentum rate of change $\dot{L}_{actual}$ of our robot (HURON) is computed using the following expression:

$$\dot{L}_{actual} = A_L \ddot{q} + \dot{A}_L \dot{q} \tag{68}$$

where A_L and $\dot{A}_L$ are the first three rows of the Centroidal Momentum Matrix (CMM) and its derivative respectively.

The second term of the objective function is **Angular Momentum Balance Term**. The desired angular momentum rate of change about the CoM is defined as

$$\dot{H}_{desired} = 0 \tag{69}$$

The actual angular momentum rate of change about the $\dot{H}_{actual}$ of our robot (HURON) is computed using the following expression:

$$\dot{H}_{actual} = A_H \ddot{q} + \dot{A}_H \dot{q} \tag{70}$$

where A_H and $\dot{A}_H$ are the last three rows of the Centroidal Momentum Matrix (CMM) and its derivative respectively.

The third term of the objective function is the **Swing Leg Trajectory Tracking Term**. It is defined to follow the desired swing leg trajectory described in section 7.1.2.2. The desired joint acceleration is

$$\ddot{\theta}_{des} = K_p(\theta_r - \theta) + K_d(\dot{\theta}_r - \dot{\theta}) + \ddot{\theta}_r \tag{71}$$

where θ_r, $\dot{\theta}_r$ and $\ddot{\theta}_r$ are the reference position, velocity and acceleration, respectively, as decribed in section 7.1.2.2.

The objective function is constrained by three constraints. The first constraint, known as the **contact constraint**, is employed to represent the interaction between the system and its surroundings. The second constraint is the **dynamic constraint**, which guarantees that the joint accelerations, in combination with the Coriolis forces, gravitational forces, and applied torques, align with

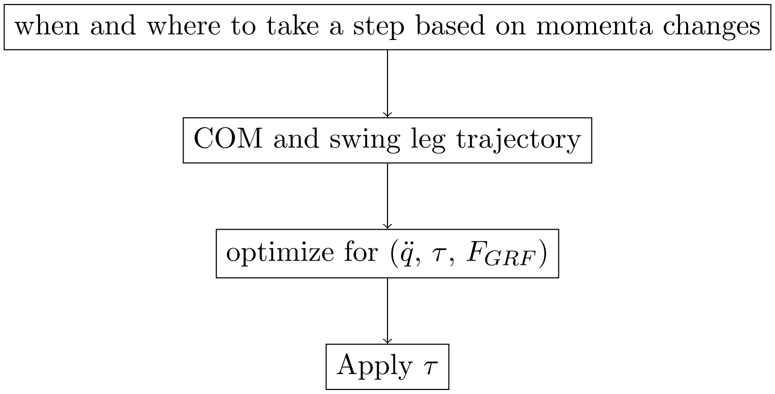

Figure 46: Block diagram of the stepping stability methodology.

the external forces exerted on the system. The external forces encompass the contact forces exerted at distinct contact points, with each foot having one contact point. For the **friction cone constraint**, the friction pyramid expands upon this concept by incorporating a pyramid shape, which more accurately represents the limitation of tangential forces in several directions [55]. The pyramid is commonly depicted as a collection of linear inequalities. The friction pyramid constraint can be mathematically stated in three-dimensional space as: ($f_{GRF,x} \leq \mu f_{GRF,z}$), ($-f_{GRF,x} \leq \mu f_{GRF,z}$), ($f_{GRF,y} \leq \mu f_{GRF,z}$), ($-f_{GRF,y} \leq \mu f_{GRF,z}$), and ($0 \leq \mu f_{GRF,z}$).

The block diagram presented in Fig. 46 illustrates the methodology employed in this study, depicting the sequential steps.

7.1.3 Stepping-Based Stability Control: Current Direction

The optimization problem, consisting of the objective function and three constraints, was effectively implemented. The optimal joint accelerations, torques and Ground Reaction Forces were determined to achieve the desired momenta and desired swing leg trajectory and satisfy the stability and dynamics constraints as shown in Fig. 47. Initially, our objective was to establish the optimization problem by assuming that the desired rate of change of linear momentum is zero, and the swing leg trajectory tracking term is set to the upright posture configuration. At present, we are in the process of implementing the desired CoM (Center of Mass) and swing leg trajectories. These trajectories will be used later to calculate the desired values of $\dot{L}_{des}$ (desired linear momentum) and $\ddot{\theta}_{des}$ (desired angular acceleration). We anticipate that the ongoing data collection and analysis processes will yield conclusive results in the coming days, further validating the efficacy of the employed methodology.

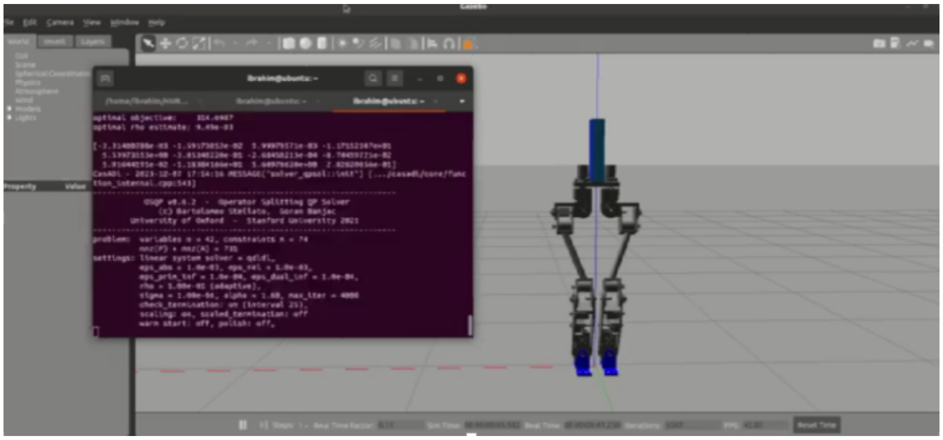

```
optimal objective:    314.0987
optimal rho estimate: 9.49e-03

[illegible]
CasADi - 2023-12-07 17:54:16 MESSAGE("solver_qpsol::init") [.../casadi/core/func
tion_internal.cpp:543]
-----------------------------------------------------------------
           OSQP v0.6.2  -  Operator Splitting QP Solver
              (c) Bartolomeo Stellato,  Goran Banjac
        University of Oxford  -  Stanford University 2021
-----------------------------------------------------------------
problem:  variables n = 42, constraints m = 74
          nnz(P) + nnz(A) = 731
settings: linear system solver = qdldl,
          eps_abs = 1.0e-03, eps_rel = 1.0e-03,
          eps_prim_inf = 1.0e-04, eps_dual_inf = 1.0e-04,
          rho = 1.00e-01 (adaptive),
          sigma = 1.00e-06, alpha = 1.60, max_iter = 4000
          check_termination: on (interval 25),
          scaling: on, scaled_termination: off
          warm start: off, polish: off,
```

Figure 47: Optimization Framework Validation: Optimal Decision Variables Meeting Momentum and Constraint Requirements.

7.2 Future Works

Our future plans include implementing our proposed push recovery control to our manufactured bipedal, HURON, once it is ready for experimental tests. Additionally, we plan to complete the current work related to push recovery via stepping.

Appendices

A Sagittal and Frontal Planes:

Sagittal Plane: A vertical plane that extends from the front to the back, dividing the body into right and left sides.

Frontal Plane: A vertical plane that divides the humanoid robot's body into front and back halves.

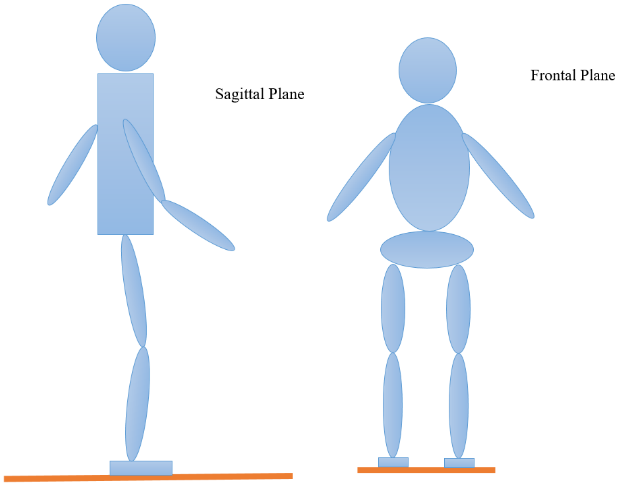

(a) (b)

Figure 48: (a) Sagittal Plane, (b) Frontal Plane.

B Inertia Matrix about the CoM about the y-axis A(q):

Preliminaries:

- CoM of multiple rigid bodies:

$$CoM = \frac{\sum m_i c_i}{\sum m_i} \tag{72}$$

.

- Parallel axis theorem:

$$I_{axis} = I_{CoM} + mr^2 \tag{73}$$

where r is the distance between the CoM and the axis.

- Linear Momentum (P) of a rigid body:

$$P = mV_{CoM} \tag{74}$$

- Angular Momentum (L) of a rigid body:

$$L = rX(mV_{CoM}) + I_{CoM}w \tag{75}$$

Notations:

- r_j: position vector of joint j w.r.t base frame.
- c_j: CoM of link directly connected to joint j.
- I_j: moment of inertia tensor of link directly connected to joint j. about the CoM of the link.
- m_j: mass of the link directly connected to joint j.
- $\dot{\theta}_j$: angular speed of joint j.
- a_j: rotation axis vector of joint j.
- w_j: angular velocity of joint j.
- $\tilde{m}_j$: mass of all links driven by joint j.
- $\tilde{c}_j$: center of mass formed by all links driven by joint j.
- $\tilde{I}_j$: total moment of inertia of all links driven by joint j.
- $\tilde{v}_{CoM,j}$: linear velocity of the CoM of all links driven by joint j.

Inertia Matrix M and A Calculation:

- $$P = M(\theta)\dot{\theta} \tag{76}$$

- $$L = A(\theta)\dot{\theta} \tag{77}$$

- The calculation of M and A is achieved recursively.

$$\tilde{m}_{j-1} = \tilde{m}_j + m_{j-1} \tag{78}$$

$$\tilde{c}_{j-1} = \frac{\tilde{m}_j \tilde{c}_j + m_{j-1} c_{j-1}}{\tilde{m}_j + m_{j-1}} \tag{79}$$

$$\tilde{I}_{j-1} = \tilde{I}_j + [0,0,0;0,0,0;0,0,\tilde{m}_j(|\tilde{c}_j - \tilde{c}_{j-1}|)^2] + I_{j-1} + [0,0,0;0,0,0;0,0,m_{j-1}(|c_{j-1} - \tilde{c}_{j-1}|)^2] \tag{80}$$

Linear momentum of a link

$$P_{j-1} = w_{j-1} X (\tilde{c}_{j-1} - r_{j-1}) \tilde{m}_{j-1} \tag{81}$$

Angular momentum of a link

$$L_{j-1} = \tilde{c}_{j-1} X (P_{j-1}) + \tilde{I}_{j-1} w_{j-1} \tag{82}$$

$$w_{j-1} = a_{j-1} \dot{\theta}_{j-1} \tag{83}$$

$$M_{j-1} = a_{j-1} X (\tilde{c}_{j-1} - r_{j-1}) \tilde{m}_{j-1} \tag{84}$$

$$A_{j-1} = \tilde{c}_{j-1} X M_{j-1} + \tilde{I}_{j-1} a_{j-1} \tag{85}$$

$$M = [M_1, M_2, M_3] \tag{86}$$

$$A = [A_1, A_2, A_3] \tag{87}$$

C Center of Pressure (CoP) Calculation:

When all the contacts between the robot feet and the ground are on a single plane, as in our case, the CoP coincides with the Zero Moment Point (ZMP) [56]. We calculated the x-component of the CoP p_x using the procedure described in [3].

Let $\mathbf{f}_L = [f_{L_x}\ f_{L_y}\ f_{L_z}]$ and $\tau_L = [\tau_{L_x}\ \tau_{L_y}\ \tau_{L_z}]$ be the output forces and torques of the left FT sensor, and $\mathbf{f}_R = [f_{R_x}\ f_{R_y}\ f_{R_z}]$ and $\tau_R = [\tau_{R_x}\ \tau_{R_y}\ \tau_{R_z}]$ be the equivalent outputs of the right FT sensor. The left and right Force/Torque sensors are placed symmetrically at positions $\mathbf{p}_L = [p_{L_x}\ p_{L_y}\ p_{L_z}]$ and $\mathbf{p}_R = [p_{R_x}\ p_{R_y}\ p_{R_z}]$, respectively. As a result:

$$p_x = \frac{\tau_{L_y} + p_{L_z} f_{L_z} + \tau_{R_y} + p_{R_z} f_{R_z}}{f_{L_x} + f_{R_x}} \tag{88}$$

$$p_y = \frac{\tau_{L_z} + p_{L_z} f_{L_y} + \tau_{R_z} + p_{R_y} f_{R_y}}{f_{L_x} + f_{R_x}} \tag{89}$$

References

[1] D. Winter, “Human balance and posture control during standing and walking,” *Gait &amp; Posture*, vol. 3, no. 4, p. 193–214, 1995.

[2] A. I. Elhasairi, M. Sweeting, and A. N. Pechev, *Humanoid robot full-body control & balance restoration.* PhD thesis.

[3] S. Kajita, H. Hirukawa, K. Harada, and K. Yokoi, *Introduction to Humanoid Robotics*, vol. 101 of *Springer Tracts in Advanced Robotics.* Berlin, Heidelberg: Springer, 2014.

[4] M. Vukobratović and J. Stepanenko, “On the stability of anthropomorphic systems,” *Mathematical Biosciences*, vol. 15, no. 1–2, p. 1–37, 1972.

[5] B. Stephens, “Integral control of humanoid balance,” in *2007 IEEE/RSJ International Conference on Intelligent Robots and Systems*, IEEE, Oct. 2007.

[6] M. Abdallah and A. Goswami, “A biomechanically motivated two-phase strategy for biped upright balance control,” in *Proceedings of the 2005 IEEE International Conference on Robotics and Automation*, IEEE, 2006.

[7] T. Koolen, T. de Boer, J. Rebula, A. Goswami, and J. Pratt, “Capturability-based analysis and control of legged locomotion, part 1: Theory and application to three simple gait models,” *The International Journal of Robotics Research*, vol. 31, no. 9, p. 1094–1113, 2012.

[8] C.-C. Wu and V. Zordan, “Goal-directed stepping with momentum control.,” pp. 113–118, 07 2010.

[9] B. Stephens, *Push Recovery Control for Force-Controlled Humanoid Robots.* PhD thesis, 2011. Copyright - Database copyright ProQuest LLC; ProQuest does not claim copyright in the individual underlying works; Last updated - 2023-03-03.

[10] W. Yu, G. Bao, and Z. Wang, “Effects of joint torque constraints on humanoid robot balance recovery in the presence of external disturbance,” *2009 IEEE International Conference on Robotics and Biomimetics (ROBIO)*, 2009.

[11] M. Vukobratovic and D. Juricic, “Contribution to the synthesis of biped gait,” *IEEE Transactions on Biomedical Engineering*, vol. BME-16, no. 1, p. 1–6, 1969.

[12] M. VUKOBRATOVIĆ and B. BOROVAC, “Zero-moment point — thirty five years of its life,” *International Journal of Humanoid Robotics*, vol. 01, no. 01, p. 157–173, 2004.

[13] J.-H. Kim, “Multi-axis force-torque sensors for measuring zero-moment point in humanoid robots: A review,” *IEEE Sensors Journal*, vol. 20, no. 3, p. 1126–1141, 2020.

[14] B. Siciliano, *Springer Handbook of Robotics.* Springer International Publishing, 2016.

[15] M. Wang, M. Ceccarelli, and G. Carbone, “A feasibility study on the design and walking operation of a biped locomotor via dynamic simulation,” *Frontiers of Mechanical Engineering*, vol. 11, no. 2, p. 144–158, 2016.

[16] B. Jalgha, D. Asmar, and I. Elhajj, “A hybrid ankle/hip preemptive falling scheme for humanoid robots,” in *2011 IEEE International Conference on Robotics and Automation*, IEEE, May 2011.

[17] H. Hemami, F. Weimer, and S. Koozekanani, “Some aspects of the inverted pendulum problem for modeling of locomotion systems,” *IEEE Transactions on Automatic Control*, vol. 18, no. 6, p. 658–661, 1973.

[18] S. Dutta, T. K. Maiti, Y. Ochi, M. Miura-Mattausch, S. Bhattacharya, N. Yorino, and H. J. Mattausch, “Stability analysis of humanoid robots with gyro sensors subjected to external push forces,” *2019 2nd International Symposium on Devices, Circuits and Systems (ISDCS)*, 2019.

[19] M. Folgheraiter, A. Yessaly, G. Kaliyev, A. Yskak, S. Yessirkepov, A. Oleinikov, and G. Gini, “Computational efficient balance control for a lightweight biped robot with sensor based zmp estimation,” *2018 IEEE-RAS 18th International Conference on Humanoid Robots (Humanoids)*, 2018.

[20] C. Li, R. Xiong, Q.-G. Zhu, J. Wu, Y.-L. Wang, and Y.-M. Huang, “Push recovery for the standing under-actuated bipedal robot using the hip strategy,” *Front. Inf. Technol. Electron. Eng.*, vol. 16, pp. 579–593, July 2015.

[21] S. Singh, “Push recovery for humanoid robots using linearized double inverted pendulum.”

[22] M. Popovic, A. Hofmann, and H. Herr, “Angular momentum regulation during human walking: Biomechanics and control,” *IEEE International Conference on Robotics and Automation, 2004. Proceedings. ICRA ’04. 2004*, 2004.

[23] S. Kajita, F. Kanehiro, K. Kaneko, K. Fujiwara, K. Harada, K. Yokoi, and H. Hirukawa, “Resolved momentum control: humanoid motion planning based on the linear and angular momentum,” in *Proceedings 2003 IEEE/RSJ International Conference on Intelligent Robots and Systems (IROS 2003) (Cat. No.03CH37453)*, IEEE, 2004.

[24] J. Park, Y. Youm, and W.-K. Chung, “Control of ground interaction at the zero-moment point for dynamic control of humanoid robots,” in *Proceedings of the 2005 IEEE International Conference on Robotics and Automation*, IEEE, 2006.

[25] A. Macchietto, V. Zordan, and C. R. Shelton, “Momentum control for balance,” *ACM Trans. Graph.*, vol. 28, pp. 1–8, July 2009.

[26] B. J. Stephens and C. G. Atkeson, “Dynamic balance force control for compliant humanoid robots,” in *2010 IEEE/RSJ International Conference on Intelligent Robots and Systems*, IEEE, Oct. 2010.

[27] A. P. Macchietto, *Momentum-based balance control for simulated characters.* PhD thesis.

[28] A. Hofmann, M. Popovic, and H. Herr, “Exploiting angular momentum to enhance bipedal center-of-mass control,” *2009 IEEE International Conference on Robotics and Automation*, 2009.

[29] Y. Pan, C. Yang, L. Pan, and H. Yu, “Integral sliding mode control: Performance, modification, and improvement,” *IEEE Trans. Industr. Inform.*, vol. 14, pp. 3087–3096, July 2018.

[30] N. Qiao, L. Wang, M. Liu, and Z. Wang, "The sliding mode controller with improved reaching law for harvesting robots," *J. Intell. Robot. Syst.*, vol. 104, Jan. 2022.

[31] C. J. Fallaha, M. Saad, H. Y. Kanaan, and K. Al-Haddad, "Sliding-mode robot control with exponential reaching law," *IEEE Trans. Ind. Electron.*, vol. 58, pp. 600–610, Feb. 2011.

[32] F. Xu, N. An, J. Mao, and S. Yang, "A new variable exponential power reaching law of complementary terminal sliding mode control," *Complexity*, vol. 2020, pp. 1–11, Oct. 2020.

[33] H. Wang, X. Zhao, and Y. Tian, "Trajectory tracking control of XY table using sliding mode adaptive control based on fast double power reaching law," *Asian J. Control*, vol. 18, pp. 2263–2271, Nov. 2016.

[34] Z. Kang, H. Yu, and C. Li, "Variable-parameter double-power reaching law sliding mode control method," *Automatika*, vol. 61, pp. 345–351, July 2020.

[35] W. Gao and J. C. Hung, "Variable structure control of nonlinear systems: a new approach," *IEEE Trans. Ind. Electron.*, vol. 40, no. 1, pp. 45–55, 1993.

[36] M. Mori and M. Sugihara, "The double-exponential transformation in numerical analysis," *J. Comput. Appl. Math.*, vol. 127, pp. 287–296, Jan. 2001.

[37] T. Ooura and M. Mori, "A robust double exponential formula for fourier-type integrals," *J. Comput. Appl. Math.*, vol. 112, pp. 229–241, Nov. 1999.

[38] P. Hsu, J. Hauser, and S. Sastry, "Dynamic Control of Redundant Manipulators," in *1988 American Control Conference*, pp. 2135–2139, June 1988.

[39] B. Siciliano and J.-J. Slotine, "A general framework for managing multiple tasks in highly redundant robotic systems," in *Fifth International Conference on Advanced Robotics 'Robots in Unstructured Environments*, pp. 1211–1216 vol.2, June 1991.

[40] Y. Nakamura, H. Hanafusa, and T. Yoshikawa, "Task-Priority Based Redundancy Control of Robot Manipulators," *The International Journal of Robotics Research*, vol. 6, pp. 3–15, June 1987. Publisher: SAGE Publications Ltd STM.

[41] J. Hollerbach and K. Suh, "Redundancy resolution of manipulators through torque optimization," *IEEE Journal on Robotics and Automation*, vol. 3, pp. 308–316, Aug. 1987. Conference Name: IEEE Journal on Robotics and Automation.

[42] O. Khatib, "Real-time obstacle avoidance for manipulators and mobile robots," in *1985 IEEE International Conference on Robotics and Automation Proceedings*, vol. 2, pp. 500–505, Mar. 1985.

[43] O. Khatib, "A unified approach for motion and force control of robot manipulators: The operational space formulation," *IEEE Journal on Robotics and Automation*, vol. 3, pp. 43–53, Feb. 1987. Conference Name: IEEE Journal on Robotics and Automation.

[44] O. Khatib, L. Sentis, J. Park, and J. Warren, "WHOLE-BODY DYNAMIC BEHAVIOR AND CONTROL OF HUMAN-LIKE ROBOTS," *International Journal of Humanoid Robotics*, vol. 01, pp. 29–43, Mar. 2004.

[45] L. Sentis and O. Khatib, "Prioritized multi-objective dynamics and control of robots in human environments," in *4th IEEE/RAS International Conference on Humanoid Robots, 2004.*, vol. 2, pp. 764–780 Vol. 2, Nov. 2004.

[46] J. Nakanishi, R. Cory, M. Mistry, J. Peters, and S. Schaal, "Operational Space Control: A Theoretical and Empirical Comparison," *The International Journal of Robotics Research*, vol. 27, pp. 737–757, June 2008.

[47] H. Cruse, E. Wischmeyer, M. Brüwer, P. Brockfeld, and A. Dress, "On the cost functions for the control of the human arm movement," *Biological Cybernetics*, vol. 62, pp. 519–528, Apr 1990.

[48] J. Pratt, J. Carff, S. Drakunov, and A. Goswami, "Capture point: A step toward humanoid push recovery," *2006 6th IEEE-RAS International Conference on Humanoid Robots*, 2006.

[49] J. Englsberger, C. Ott, M. A. Roa, A. Albu-Schaffer, and G. Hirzinger, "Bipedal walking control based on capture point dynamics," *2011 IEEE/RSJ International Conference on Intelligent Robots and Systems*, 2011.

[50] M. Krause, J. Englsberger, P.-B. Wieber, and C. Ott, "Stabilization of the capture point dynamics for bipedal walking based on model predictive control," *IFAC Proceedings Volumes*, vol. 45, no. 22, p. 165–171, 2012.

[51] S. Dafarra, F. Romano, and F. Nori, "Torque-controlled stepping-strategy push recovery: Design and implementation on the iCub humanoid robot," in *2016 IEEE-RAS 16th International Conference on Humanoid Robots (Humanoids)*, pp. 152–157, Nov. 2016. ISSN: 2164-0580.

[52] S. Kudoh, T. Komura, and K. Ikeuchi, "Stepping motion for a human-like character to maintain balance against large perturbations," in *Proceedings 2006 IEEE International Conference on Robotics and Automation, 2006. ICRA 2006.*, 2006.

[53] S. Jain, Y. Ye, and C. K. Liu, "Optimization-based interactive motion synthesis," *ACM Transactions on Graphics*, vol. 28, no. 1, p. 1–12, 2009.

[54] C.-C. Wu, J. Medina, and V. B. Zordan, "Simple steps for simply stepping," *Advances in Visual Computing*, p. 97–106, 2008.

[55] K. Bouyarmane, S. Caron, A. Escande, and A. Kheddar, "Multi-contact motion planning and control," *Humanoid Robotics: A Reference*, p. 1–42, 2017.

[56] P. Sardain and G. Bessonnet, "Forces acting on a biped robot. center of pressure-zero moment point," *IEEE Transactions on Systems, Man, and Cybernetics - Part A: Systems and Humans*, vol. 34, no. 5, pp. 630–637, 2004.